

For Reference

NOT TO BE TAKEN FROM THIS ROOM

Thesis
1969(F)
117

For Reference

NOT TO BE TAKEN FROM THIS ROOM

Ex LIBRIS
UNIVERSITATIS
ALBERTAENSIS



Regulations Regarding Theses and Dissertations

[illegible]



Digitized by the Internet Archive
in 2019 with funding from
University of Alberta Libraries

<https://archive.org/details/Humphries1969>

Thesis
1969(F)
117

THE UNIVERSITY OF ALBERTA

ELASTIC SCATTERING OF ^3He ON s-d SHELL NUCLEI

by



Robert Gordon Humphries

A THESIS

SUBMITTED TO THE FACULTY OF GRADUATE STUDIES

IN PARTIAL FULFILLMENT OF THE REQUIREMENTS FOR THE DEGREE

OF MASTER OF SCIENCE

DEPARTMENT OF PHYSICS

EDMONTON, ALBERTA

Fall, 1969

UNIVERSITY OF ALBERTA
FACULTY OF GRADUATE STUDIES

The undersigned certify that they have read, and recommend to the Faculty of Graduate Studies for acceptance, a thesis entitled ELASTIC SCATTERING OF ^3He ON s-d SHELL NUCLEI, submitted by Robert Gordon Humphries in partial fulfillment of the requirements for the degree of Master of Science.

THE HISTORY OF THE

REIGN OF KING CHARLES THE FIRST

IN WHICH ARE CONTAINED THE MOST IMPORTANT AND INTERESTING

EVENTS OF HIS REIGN, FROM THE BEGINNING OF HIS REIGN, TO THE

END OF HIS REIGN, AND THE DEATH OF HIS SON, KING CHARLES THE SECOND.

BY JOHN HUME, ESQ. OF THE BARR, AND OF THE HOUSE OF COMMONS.

LONDON: Printed by J. B. 1719.

ABSTRACT

The angular distributions for the elastic scattering reactions $^{19}\text{F}(^3\text{He}, ^3\text{He})^{19}\text{F}$, $^{23}\text{Na}(^3\text{He}, ^3\text{He})^{23}\text{Na}$, $^{27}\text{Al}(^3\text{He}, ^3\text{He})^{27}\text{Al}$ and $^{28}\text{Si}(^3\text{He}, ^3\text{He})^{28}\text{Si}$ have been measured from 30° to 160° at bombarding energies of 5.0 MeV and 6.5 MeV. The absolute cross-sections were measured for the 5.0 MeV distributions and estimates of the absolute cross-sections for the 6.5 MeV data were obtained from optical model calculations. Optical model parameters were determined by fitting the elastic distributions with the aid of an optical model search program written by Perey. It was not possible to determine a unique set of parameters for each elastic scattering reaction.

ACKNOWLEDGEMENTS

I wish to express my gratitude to Dr. G. Roy, who not only suggested the project but designed an excellent charged particle system on which the experiments were carried out.

I would especially like to thank the members of 'Magpak': Jan Bogaards, Norm Davison and Bill Saunders, for helping take the data and for their helpful suggestions and ideas during its analysis. They were a most friendly and cooperative group of people to work with.

I also thank the Postdoctoral Fellows and Research Associates here at the Nuclear Research Center, for taking the time to answer and discuss the many questions I had with regard to the project and nuclear physics in general.

I am very grateful to Mr. Jock Elliott and the other members of the technical and secretarial staff at the laboratory, for their friendly cooperation and good-natured response to my various antics. It has indeed been a pleasure to know the various people associated with the Nuclear Research Center during my studies there.

I am indebted to Miss Elsie Hawirko for managing to type this thesis so carefully from my barely discernible notes.

I wish to thank my family for their support and understanding during the time I spent at the University of Alberta obtaining my degrees.

Finally, I wish to gratefully acknowledge the financial support of the National Research Council and of the University of Alberta.

TABLE OF CONTENTS

	Page
INTRODUCTION	1
CHAPTER 1 THE OPTICAL MODEL	3
1.1 Development	3
1.2 The One-dimensional Case	7
1.3 Scattering Theory	9
1.4 Optical Model Calculations	12
1.5 Charged Particles	14
1.6 Spin Effects	15
1.7 Non-local Potentials	16
1.8 Deformed Nuclei	17
1.9 Form Factors	17
1.10 Fitting Procedure	19
1.11 Ambiguities	19
1.12 Limitations	20
1.13 Applications of the Optical Model	21
CHAPTER 2 EXPERIMENTAL	23
2.1 Scattering Chamber	23
2.2 Target Biaser	25
2.3 Targets and Target Preparation	26
2.4 Relative Cross-Section Measurements	27
2.5 Absolute Cross-Sections	28
2.6 Data Reduction	29
CHAPTER 3 ANALYSIS AND RESULTS	31
3.1 Compound Nucleus Contribution	31
3.2 Excitation Curves	33

	Page
3.3 Angular Distributions	34
3.4 Fitting Procedure	39
3.5 Results and Conclusions	42
Fluorine	43
Sodium	43
Aluminum	44
Silicon	44

REFERENCES

1. J. J. Griffin, *Journal of Sound and Vibration*, **15**, 1 (1971).
2. J. J. Griffin, *Journal of Sound and Vibration*, **15**, 1 (1971).
3. J. J. Griffin, *Journal of Sound and Vibration*, **15**, 1 (1971).
4. J. J. Griffin, *Journal of Sound and Vibration*, **15**, 1 (1971).
5. J. J. Griffin, *Journal of Sound and Vibration*, **15**, 1 (1971).
6. J. J. Griffin, *Journal of Sound and Vibration*, **15**, 1 (1971).
7. J. J. Griffin, *Journal of Sound and Vibration*, **15**, 1 (1971).
8. J. J. Griffin, *Journal of Sound and Vibration*, **15**, 1 (1971).
9. J. J. Griffin, *Journal of Sound and Vibration*, **15**, 1 (1971).
10. J. J. Griffin, *Journal of Sound and Vibration*, **15**, 1 (1971).

LIST OF FIGURES

		Following Page:
1.1	An optical model potential	18
2.1	Photograph of the charged particle system	23
2.2	A typical spectrum	24
3.1	Excitation curves for ^{19}F	33
3.2	Excitation curves for ^{23}Na	33
3.3	Excitation curves for ^{27}Al	33
3.4	Excitation curves for ^{28}Si	33
3.5	Plot of real and imaginary phase shifts, vs ℓ for the elastic scattering of helions at 6.5 MeV on ^{19}F	44
3.6	Elastic scattering distributions and optical model fits for ^{19}F	46
3.7	Elastic scattering distributions and optical model fits for ^{23}Na	46
3.8	Elastic scattering distributions and optical model fits for ^{27}Al	46
3.9	Elastic scattering distributions and optical model fits for ^{28}Si	46

LIST OF TABLES

	Page
Table 3.1 Level density parameters for Hauser-Feshbach calculations	32
Table 3.2 Absolute cross-sections and σ/σ_R for $^{19}\text{F}(^3\text{He}, ^3\text{He})^{19}\text{F}$ at 5.0 MeV and 6.5 MeV	35
Table 3.3 Absolute cross-sections and σ/σ_R for $^{23}\text{Na}(^3\text{He}, ^3\text{He})^{23}\text{Na}$ at 5.0 MeV and 6.5 MeV	36
Table 3.4 Absolute cross-sections and σ/σ_R for $^{27}\text{Al}(^3\text{He}, ^3\text{He})^{27}\text{Al}$ at 5.04 MeV and 6.5 MeV	37
Table 3.5 Absolute cross-sections and σ/σ_R for $^{28}\text{Si}(^3\text{He}, ^3\text{He})^{28}\text{Si}$ at 5.04 MeV and 6.5 MeV	38
Table 3.6 Helion optical model parameter sets	46

INTRODUCTION

The purpose of this study was to determine optical model parameters, from the elastic scattering of ^3He at Van de Graaff energies, for several nuclei in the first half of the s-d shell. The study of helion[†] elastic scattering is comparatively recent as most investigations were started after 1960. Of these studies, the majority were done for tandem energies or higher and as a result there are few optical model parameters available for the lighter nuclei below 8.0 MeV.

Recently at the Nuclear Research Center of the University of Alberta, several ($^3\text{He},n$) reactions have been investigated and proposed (Ho 69, Hs 68, Sh 69). Since there is considerable interest in helion induced reactions at this laboratory it was thought that a worthwhile study would be to obtain the helion optical model parameters for several nuclei of interest. Thus the helion elastic scattering angular distribution were taken for ^{19}F , ^{23}Na , ^{27}Al and ^{28}Si at bombarding energies of 5.0 MeV and 6.5 MeV. The optical model parameters are necessary for the distorted wave Born approximation (DWBA) analysis of the stripping data.

Compound nucleus calculations, for the various reactions studied at the University of Alberta, are frequently carried out via Hauser-Feshbach analysis (Da 69a, Sm 67). Since the optical model parameters for all

[†]The new notation 'helion' proposed by Bromley (Br 67) will be used for the ^3He ion.

possible exit channels are needed for the calculations, the helion parameters obtained from this study will also be useful for this purpose.

The thesis has three chapters: Theoretical, Experimental, and Results and Conclusions. The chapter on theory will attempt to present the basic ideas and methods of the optical model without a rigorous mathematical development. There are several excellent papers and texts available (Br 59, Ho 63, Ro 61, Ul 64) which give a more detailed presentation than is possible here.

The experimental chapter will discuss the new charged particle scattering chamber that was installed at the beginning of this project. The purpose of this description will be to acquaint someone using it for the first time with the experimental techniques involved in using the system.

In the last chapter, the compound nucleus calculations, excitation curves and optical model parameter searches and results will be discussed.

CHAPTER 1

THE OPTICAL MODEL

1.1 Development

At the present time there is no consistent theory of the nucleus which will allow us to compute the parameters of a nuclear reaction, eg. the transition probabilities and spectroscopic factors. Our only alternative therefore, is to build model representations of the nucleus and thus find the parameters of the given nuclear model instead of looking for the transition probability of every single event by experiment. If we had a suitable model of a nucleus then one could theoretically predict the values of cross-sections for nuclear reactions. However, the investigation of the nuclear reaction is developing simultaneously with the search for a simple model, which would satisfactorily explain these processes.

In this chapter the optical model will be discussed, its development, use, and interesting features. There will be no rigorous mathematical development of the formulae used as this is done fully in several books and papers on the optical model. Instead the overall picture will be sketched and simplifications such as considering uncharged spinless particles will be used when necessary with generalizations to the more realistic case indicated.

The first theoretical considerations of nuclear reactions (Be 37) concerned neutron induced reactions and were based on the shell model

concept of the nucleus with a rectangular well form of potential

$$\begin{aligned} V(r) &= -V_0 & r \leq a \\ V(r) &= 0 & r > a \end{aligned} \quad 1.1$$

where a is the radius of the nucleus. This model implies that the elastic scattering will be prevalent and that the cross-sections are expected to have resonance maxima corresponding to a few stationary nuclear levels situated far from each other.

The possibility of using this model for the explanation of a nuclear reaction was disproved with the discovery of resonance capture of slow neutrons by nuclei. It could be shown that the resonance levels lie quite close together (in the energy scale) and are connected with values of the cross-sections for inelastic scattering and the proper nuclear reaction.

Subsequently the compound nucleus model was proposed by N. Bohr (Bo 36) to describe the nuclear reaction. In this model, the interaction between the nucleus and incident particle is presumed to be so strong that the nucleon is absorbed by the nucleus. Thus the reaction is thought to proceed in two stages. First, the incident particle is captured by the nucleus and forms a non-stable compound nucleus. Secondly, there is the decay of the compound nucleus, which is independent of the first stage, but only depends on the properties of the compound nucleus itself. Therefore, every process, including elastic scattering, passes through the compound nucleus. In this theory, the Breit-Wigner formula (Br 36) describes the dependence of the cross-sections on energy in the neighbourhood of the

resonance energies, which are interpreted as energy levels of the compound nucleus.

A conclusion of the compound nucleus model is that the energy of the captured particle is distributed almost immediately among the other nucleons and as a result the particles, emitted from the nucleus during the reaction, should have a much smaller energy to that of the incident particles. This means the energy spectrum of the outgoing particles ought to be close to the Maxwellian spectrum. Also since both stages of the reaction are mutually independent, the angular distribution of the emitted particles ought to be isotropic.

These conclusions have been demonstrated experimentally in many cases but there are also many reactions in which the particles are emitted anisotropically, with emission in the forward direction prevalent. It was found however, that in other reactions inelastic scattering predominates with small differences between the energies of incident and emitted particles. These experiments indicate that a nucleon can be captured by a nucleus but this does not imply the formation of a compound nucleus.

Thus we see that an agreement between the theoretical conclusions and the empirical data could not be gained by these and other experiments. In the range of small energies, the position of the resonance maxima of the cross-sections was in principle impossible to determine. It was expected however, that in the higher energy ranges, the energy spectrum of the compound nucleus would practically be continuous and therefore the cross-sections would not change considerably with the energy. A model of the

compound nucleus which would be suitable, especially for higher energies was proposed by Feshbach and Weisskopf (Fe 49). It was called the continuum model and considered the nucleus as a perfectly black nucleus. The elastic and reaction cross-sections will then have the value (U1 64)

$$\sigma_{el} = \sigma_r = \pi \left(a + \frac{1}{k} \right)^2 \quad 1.2$$

where a is the radius of the nucleus and $k^2 = 2\mu E$ with μ being the reduced mass. For incident particles of large energies we have

$$\sigma_{el} = \sigma_r \approx \pi a^2 \quad 1.3$$

It was found however, that for reactions with neutrons at energies of ~90 MeV the cross-sections differed systematically from the geometrical cross-sections. Therefore, Feshbach, Porter and Weisskopf (Fe 54) proposed that the nucleus should be considered as partly transparent and not perfectly black. This is called the optical model of the atomic nucleus, and in it the interaction of incident particle and nucleus is described by a complex potential well. This corresponds to the motion of a particle in a homogeneous medium with a complex index of refraction. The optical model is intermediate between the continuum model and the shell model of the nucleus. If the imaginary part of the potential becomes zero, the shell model is obtained, and if the ratio between the imaginary and real part of the potential tends to infinity, the continuum model results.

Weisskopf (We 56) then proposed that a nuclear reaction should be considered as a process passing through three stages. In the first stage

the incident particle is either absorbed or elastically scattered. A compound system or compound nucleus is a result of the absorption. A compound system refers to an incident particle which interacts with part of the nucleons on the surface, or induces a collective excitation of the whole nucleus. The third stage is the decay of the compound system or nucleus which may emit a particle with the same energy as the original one. Therefore elastic scattering is composed of the primary and secondary scattering.

The optical model describes only the first stage of the nuclear reaction. The real part of the optical potential leads to primary elastic scattering. The imaginary part determines the effective absorption of the incident particle by the nucleus which then leads to inelastic scattering, proper nuclear reactions and secondary elastic scattering. Although the optical model is basically phenomenological, the development of the theory has shown it to be one of the good approximations in the many-body problem.

1.2 The One-dimensional Case

To see the effect of a complex potential, we shall look briefly at the one-dimensional case before generalizing the situation. Consider the potential

$$V = - (V_0 + i W) \quad 1.4$$

where V_0 and W are positive real numbers. The Schrödinger equation with this potential for the one-dimensional case is

$$\frac{d^2\psi}{dx^2} + \frac{2m}{\hbar^2} (E + V_0 + i W) \psi = 0 . \quad 1.5$$

The plane wave solutions are of the form

$$\psi = \exp (\pm i K_C x) \quad 1.6$$

where the complex wave number K_C is given by

$$K_C = \left(\frac{1}{\hbar} \right) \sqrt{2m (E + V_0 + i W)} . \quad 1.7$$

This may be rewritten so that K_C is expressed as

$$K_C = K + ik \quad 1.8$$

where if $E + V_0 \gg W$, we have

$$\begin{aligned} K &\approx \left(\frac{1}{\hbar} \right) \sqrt{2m (E + V_0)} \\ k &\approx \frac{WK}{2 (E + V_0)} . \end{aligned} \quad 1.9$$

Substituting K_C back into the expression for ψ and choosing the plus sign for a wave moving in the positive x-direction we find that

$$\psi = e^{iKx} e^{-kx} \quad 1.10$$

which is an exponentially decaying wave. What this means is that as far as the world outside the nucleus is concerned, the particle may disappear into the nucleus but the decaying wave function cannot describe what happens inside the nucleus.

1.3 Scattering Theory

Before going further we briefly review some of the results of scattering theory and look at the modifications necessary before they are used in the optical model. A detailed derivation can be found in most nuclear physics text books (En 66, Ro 67). Beyond the nuclear region we have that the asymptotic wave function for the scattering problem is

$$\psi_{r \rightarrow \infty} = \sum_{\ell=0}^{\infty} \frac{P_{\ell}(\cos \theta)}{2 i K r} (2\ell + 1) [e^{-i K r} (-1)^{\ell+1} + S_{\ell} e^{i K r}] \quad 1.11$$

where the first term represents an ingoing spherical wave and the second term the outgoing wave. This wave function differs from that of a free particle by the factor $S_{\ell} = e^{i \eta_{\ell}}$ where η_{ℓ} is the phase shift in the ℓ -th partial wave of the divergent spherical wave. The differential cross-section for elastic scattering is

$$\frac{d\sigma_{el}}{d\Omega} = \frac{1}{4K^2} \left| \sum_{\ell=0}^{\infty} (2\ell+1) (S_{\ell}-1) P_{\ell}(\cos \theta) \right|^2 \quad 1.12$$

and the cross-sections are given by

$$\begin{aligned} \sigma_{el} &= \frac{\pi}{K^2} \sum_{\ell} (2\ell+1) |1-S_{\ell}|^2 \\ \sigma_r &= \frac{\pi}{K^2} \sum_{\ell} (2\ell+1) (1-|S_{\ell}|^2) \\ \sigma_T &= \frac{2\pi}{K^2} \sum_{\ell} (2\ell+1) (1-\text{Re } S_{\ell}) \end{aligned} \quad 1.13$$

In the above σ_{el} is the elastic cross-section, σ_r the reaction cross-section and $\sigma_T = \sigma_{el} + \sigma_r$ is the total cross-section.

In the low energy region the energy spectrum, in many cases, shows

a fine resonance structure and thus the actual cross-sections may fluctuate rapidly as a function of energy. Since in the optical model we have replaced the many-body problem by that of the motion of one particle in a medium defined by an average potential, the computed cross-sections will therefore correspond to certain average values of the measured cross-section. The resonance structure can only be gained by a genuine nuclear theory. Experimentally this averaging can be done by having poor beam resolution so that several resonances are overlapped. At higher energies the resonances are so close together that they overlap and thus only an average cross-section can be measured. Therefore, since the optical model cannot be expected to describe the fine resonance structure in the cross-sections we must average these cross-sections over an energy interval, ϵ , in the following manner

$$\langle \sigma \rangle = \frac{1}{\epsilon} \int_{E - 1/2 \epsilon}^{E + 1/2 \epsilon} \sigma(E') dE' \quad 1.14$$

If we do this to equations 1.12 and 1.13, we get

$$\begin{aligned} \langle \sigma_{el} \rangle &= \frac{\pi}{K^2} \sum_{\ell} (2\ell+1) [|1 - \langle S_{\ell} \rangle|^2 + (\langle |S_{\ell}|^2 \rangle - |\langle S_{\ell} \rangle|^2)] \\ \langle \sigma_r \rangle &= \frac{\pi}{K^2} \sum_{\ell} (2\ell+1) [1 - |\langle S_{\ell} \rangle|^2 - (\langle |S_{\ell}|^2 \rangle - |\langle S_{\ell} \rangle|^2)] \\ \langle \sigma_T \rangle &= \frac{\pi}{K^2} \sum_{\ell} (2\ell+1) [|1 - \langle S_{\ell} \rangle|^2 + 1 - |\langle S_{\ell} \rangle|^2] \end{aligned} \quad 1.15$$

where $\frac{1}{K^2}$ is taken to be constant over the interval.

The shape elastic cross-section, σ_{se} , which depends on the averaged $\langle S_{\ell} \rangle$ and the compound elastic fluctuation cross-section, σ_{ce} , are defined as

$$\begin{aligned}\sigma_{se} &= \frac{\pi}{K^2} \sum_{\ell} (2\ell+1) |1 - \langle S_{\ell} \rangle|^2 \\ \sigma_{ce} &= \frac{\pi}{K^2} \sum_{\ell} (2\ell+1) [\langle |S_{\ell}|^2 \rangle - |\langle S_{\ell} \rangle|^2] .\end{aligned}\tag{1.16}$$

The shape elastic cross-section corresponds to direct elastic scattering without the formation of the compound nucleus. The cross-section for the formation of the compound nucleus is defined as

$$\sigma_c = \frac{\pi}{K^2} \sum_{\ell} (2\ell+1) [1 - |\langle S_{\ell} \rangle|^2] .\tag{1.17}$$

Comparing the last 6 expressions we can write

$$\begin{aligned}\langle \sigma_{el} \rangle &= \sigma_{se} + \sigma_{ce} \\ \langle \sigma_r \rangle &= \sigma_c - \sigma_{ce} \\ \langle \sigma_T \rangle &= \sigma_{se} + \sigma_c .\end{aligned}\tag{1.18}$$

The shape elastic scattering is obtained from the interaction of the incident wave with the real part of the optical potential. The compound elastic scattering, which is a result of the decay of the compound nucleus, is not predictable in detail by the optical model.

Because of the averaging process involved in the calculations of the optical model, the averaged phase shifts obtained from the complex potential give $\langle S_{\ell} \rangle$. Knowing this and comparing the previous results we see that the optical model calculations predict the shape elastic cross-section, σ_{se} , instead of the elastic cross-section $\langle \sigma_{el} \rangle$, and the cross-section σ_c for the formation of the compound nucleus, instead of the reaction cross-section $\langle \sigma_r \rangle$. Since we measure experimentally $\langle \sigma_{el} \rangle$ we must have that

$\sigma_{ce} \ll \sigma_{se}$ before we can compare the experimental results with the optical model or we must have some method of determining σ_{ce} .

From the expressions for the cross-sections we see that, in comparing the optical model with experiment, the major obstacle lies in the calculation of the matrix elements S_ℓ for each partial wave from the assumed form of the two-body potential. The basic procedure for determining the S_ℓ will now be outlined.

1.4 Optical Model Calculations

The problem is that of finding the solution of the Schrödinger wave equation for the interaction

$$\nabla^2 \psi + \frac{2\mu}{\hbar^2} (E - V) \psi = 0 \quad 1.19$$

that has the required asymptotic form. We shall, for the moment, consider the simplest case of a spinless neutral particle scattering on a spherical target nucleus, also without spin, and assume local forces without momentum or isotopic spin dependence. The optical potential can therefore be written as

$$V(r) = Uf(r) + i Wg(r) \quad 1.20$$

which depends only on the position of the incident particle, and not on the positions of the nucleons in the target nucleus.

First we expand the wave function ψ in Legendre polynomials

$$\psi = \sum_{\ell} \frac{u_{\ell}(r)}{r} P_{\ell}(\cos \theta) \quad (\ell = 0, 1, 2, \dots) \quad 1.21$$

where $u_\ell(r)$ is the radial wave function for the ℓ -th partial wave, and then substitute this into the Schrödinger equation multiply by $P_m(\cos \theta)$ from the left, and integrate over the angular variables to get

$$\frac{d^2 u_\ell}{dr^2} + \left\{ \frac{2u}{\hbar^2} (E - V(r)) - \frac{\ell(\ell+1)}{r^2} \right\} u_\ell = 0. \quad 1.22$$

Setting $\rho = Kr$, where the wave number $K = \sqrt{2uE}/\hbar$ we obtain

$$\frac{d^2 u_\ell}{d\rho^2} + \left\{ 1 - \frac{V(r)}{E} - \frac{\ell(\ell+1)}{\rho^2} \right\} u_\ell = 0. \quad 1.23$$

Since $V(r)$ is complex the solution of this equation is complex. Up to a radius ρ_M , where the nuclear field is negligible, the solution of this equation inside the nucleus is obtained by numerical integration. Beyond the radius ρ_M $V(r)$ may be omitted and the asymptotic form of the radial wave function is (Sc 55)

$$U_\ell(\rho) \sim F_\ell(\rho) + i G_\ell(\rho) + S_\ell \{ F_\ell(\rho) - i G_\ell(\rho) \} \quad 1.24(a)$$

where

$$F_\ell(\rho) = \rho j_\ell(\rho) \quad \text{and} \quad G_\ell(\rho) = -\rho \eta_\ell(\rho), \quad 1.24(b)$$

$j_\ell(\rho)$ and $\eta_\ell(\rho)$ are spherical Bessel and Neumann functions.

Thus the internal solution is found by numerical integration, and the external one is known except for the complex amplitude S_ℓ . The condition that the wave function and its derivative are continuous over the boundary suffices to determine S_ℓ . Therefore, matching the logarithmic derivatives of the internal and external partial waves at the radius ρ_M will determine the S_ℓ 's which in turn are substituted into the expressions for the cross-

sections. In practice, we need only consider the partial waves up to a value $\ell = \ell_{\max}$ as larger values of ℓ do not contribute significantly.

1.5 Charged Particles

In the case of charged particles, we must also consider the Coulomb potential

$$V_C(r) = \begin{cases} \frac{Z_I Z_T e^2}{2 R_C} (3 - r^2/R_C^2) & \text{for } r < R_C \\ \frac{Z_I Z_T e^2}{r} & \text{for } r > R_C \end{cases} \quad 1.25$$

where $R_C = r_c \frac{1}{A^{1/3}}$ is the Coulomb radius and Z_I and Z_T are the charges of the incident particle and target nucleus.

Since the Coulomb field falls off slowly with distance, the scattered waves are distorted by it even at large distances. The internal wave equation now becomes

$$\frac{d^2 u_\ell}{d\rho^2} + \left\{ 1 - \frac{2u Z_I Z_T e^2}{K\hbar^2 \rho} - \frac{\ell(\ell+1)}{\rho^2} \right\} u_\ell = 0 \quad 1.26$$

which has the regular and irregular Coulomb functions as solutions.

The logarithmic derivative of the internal wave equation is obtained by numerical integration of the equation

$$\frac{d^2 u_\ell}{d\rho^2} + \left\{ 1 - \frac{V_C(\rho)}{E} - \frac{\dot{V}(\rho)}{E} - \frac{\ell(\ell+1)}{\rho^2} \right\} u_\ell = 0. \quad 1.27$$

Matching the logarithmic derivatives of the external and internal wave functions at the boundary again yields the differential elastic and

absorption cross-sections. However, since the Coulomb differential cross-section diverges for small θ , $\langle\sigma_{el}\rangle$ and $\langle\sigma_T\rangle$ cannot be defined for the scattering of charged particles.

1.6 Spin Effects

If we now consider that the incident particle has a spin the problem becomes considerably more complicated. The wave function for the incident particle must now be expanded in terms of radial, angular, and spin functions and we must now include a spin-dependent potential so that

$$V(r) = V_c(r) + Uf(r) + i W g(r) + (U_s + i W_s) h(r) \underline{\ell} \cdot \underline{\sigma}, \quad 1.28$$

where U_s and W_s are the real imaginary spin-dependent potentials, $h(r)$ is their radial variation and $\underline{\sigma}$ is the Pauli spin operator. For spin one-half particles the Schrödinger equation separates into two radial wave equations since the spin of the incident particle can couple in two ways to the orbital angular momentum ℓ to give the total angular momentum $J = \ell \pm 1/2$. For particles of unit spin, there are three radial wave equations since the spin can couple to the orbital angular momentum to give $j = \ell-1, \ell, \ell+1$. The method of solution is basically the same as before except now we have to determine S_ℓ^+ and S_ℓ^- for spin one-half particles and $S_\ell^+, S_\ell^0, S_\ell^-$ for unit spin particles.

Such things as isotopic spin and target spin can also be taken into account but it is found that these do not make a significant contribution.

1.7 Non-local Potentials

Studies have shown (Be 56, Fe 58, Su 59, Na 60) that the optical model potential, when derived as the summation of two-body potentials, is non-local in character. This takes account of the finite size of the incident particle and the dispersive nature of nuclear matter. That is, the potential acting on a particle centered at a point \underline{r} depends not only on \underline{r} but also on the value of the wave function throughout all space. The term $V(\underline{r}) \psi(\underline{r})$ in the Schrödinger equation describing the interaction (eq. 1.19) becomes

$$\int V(\underline{r}, \underline{r}') \psi(\underline{r}') d\underline{r}' \quad 1.29$$

where $V(\underline{r}, \underline{r}')$ is the non-local potential. Since the nuclear forces are of short range it is expected that the non-locality is not very large and thus the above integral is concentrated in the region $\underline{r} \sim \underline{r}'$. The Schrödinger wave equation describing the scattering by a potential that is partly local and partly non-local but spin-independent may be written as

$$(\nabla^2 + V_L(\underline{r}) - V_C(\underline{r}) + E) \psi(\underline{r}) + \int V(\underline{r}, \underline{r}') \psi(\underline{r}') d\underline{r}' = 0 \quad 1.30$$

where $V_L(\underline{r})$ is the local potential and $V_C(\underline{r})$ the Coulomb potential. Very little is known about the form of this potential but its basic characteristics have been determined (Br 57) so that it is possible to solve the non-local wave equation exactly. This, however, is quite complicated and further it has been found that the cross-sections given by a non-local potential can be accurately fitted with a purely local potential. This indicates that several simplifying approximations can be made. Perey and

Buck (Pe 62) developed an approximate solution of the non-local wave equation. If 'b' is the range of non-locality then the non-local wave function can be approximated by

$$\psi_{NL}(r) = \left(1 + \frac{mb^2}{4h^2} U_L(r) \right)^{-\frac{1}{2}} \psi_L(r) \quad 1.31$$

where $U_L(r)$ is the real part of the local potential, m is the particle mass and $\psi_L(r)$ is the local wave function. Thus in the non-local approximation the wave function is damped inside the nucleus and is unchanged outside, as $U_L(r) \rightarrow 0$.

1.8 Deformed Nuclei

So far we have only considered spherically symmetric potentials but many nuclei are known to be deformed and this can be taken into account by using a suitable deformed potential (Sh 59). With a deformed nucleus it is possible to have inelastic scattering take place which will excite collective states in the target nucleus. As this type of inelastic scattering takes place without any rearrangement of the target nucleons it is analogous to elastic scattering and cannot therefore be included in the imaginary part of the potential as is done when many inelastic reaction processes contribute to the interaction.

1.9 Form Factors

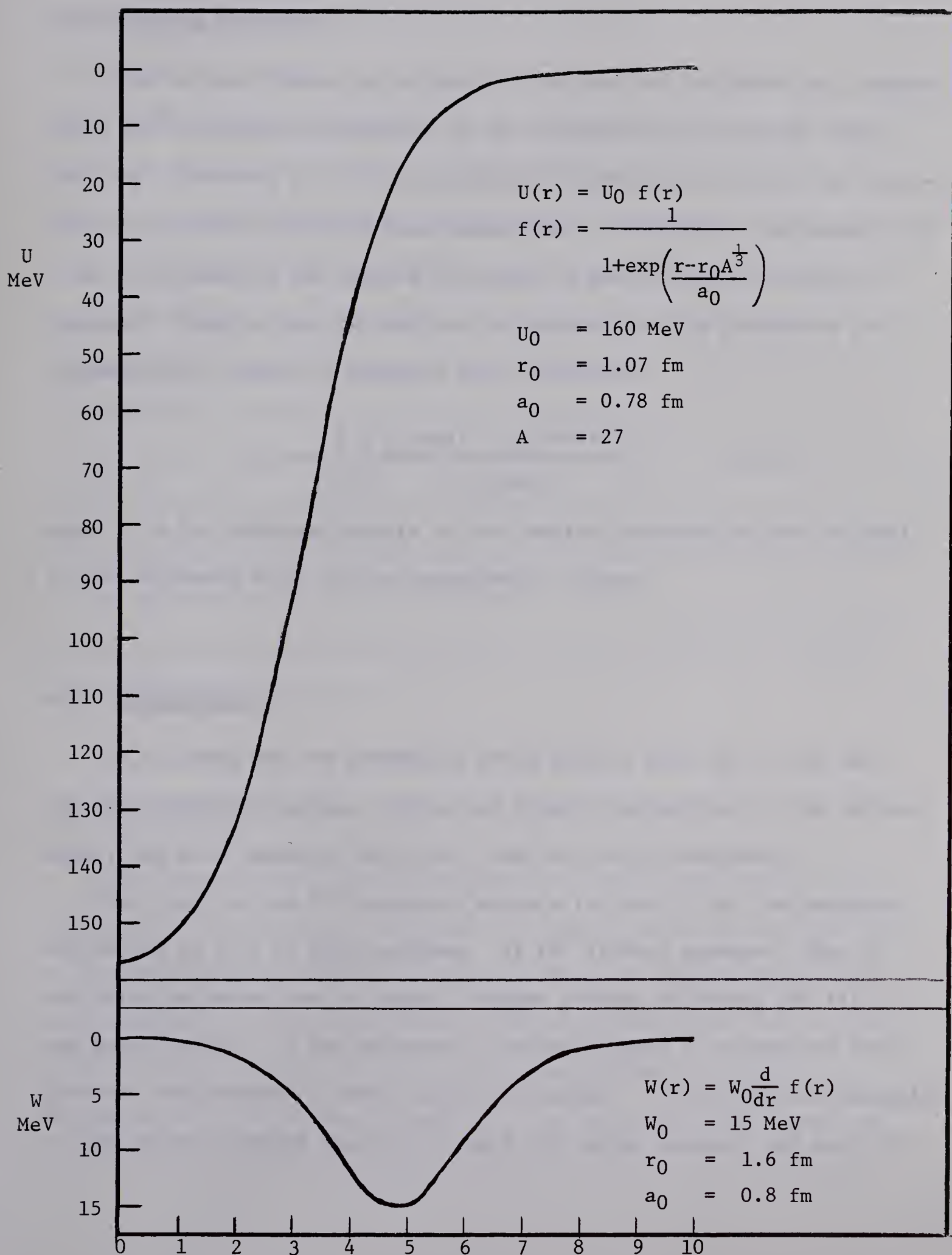
The next question to consider is the form of the radial dependence of

the potential. It is well known that charge and mass are distributed in the nucleus in such a way that their density can be described by a continuous function of the radius. It has been found experimentally that this function can be expressed as (Ho 56)

$$\rho(r) = \frac{\rho_0}{1 + \exp \left\{ \frac{(r-r_1)}{a'} \right\}} \quad 1.32$$

where ρ_0 is the constant density in the center of the nucleus, r_1 the distance from the center of the nucleus to where the density decreases to half the density value ρ_0 , and a' is the distance in which the density drops from $0.9 \rho_0$ to $0.1 \rho_0$. One can reasonably assume that the potential will show a similar radial dependence as the mass distribution. This form factor for the optical potential is known as the Saxon-Woods potential (Wo 54). However, most optical model analysis is relatively insensitive to the radial variation chosen. As long as the potential falls exponentially at large distances and is parameterized by a radius and a surface diffuseness, almost any form for the radial variation may, and has been taken (Ul 64) without significantly affecting the quality of the fit. Since it is phenomenological in nature there is no reason why the imaginary part of the potential should have the same radial variation as the real part. Indeed the Pauli principle inhibits absorption inside the nucleus at low energies, thus yielding a surface peaking which becomes less important at higher energies. Therefore it is usual, in the case of deuteron scattering for example, to use the Saxon-Woods form for the real potential and a surface form, such as the derivative of the Saxon-Woods form, for the imaginary potential.

Figure 1.1 A typical optical model potential with a Saxon-Woods form for the real part and a derivative Saxon-Woods form for the imaginary part.



1.10 Fitting Procedure

Once we have chosen the values for the real and imaginary well depths, radii and diffuseness parameters we can calculate the resulting cross-sections. However, it is not possible to reverse the procedure and calculate the potential from the experimental data. Therefore, one begins with a set of parameters and adjusts them until a good fit with the data is obtained. Usually this is done with a computer and the parameters are systematically varied to minimize the χ^2 function

$$\chi^2 = \sum_{i=1}^n \left\{ \frac{\sigma_i(\text{exp}) - \sigma_i(\text{theory})}{\Delta\sigma_i(\text{exp})} \right\}^2 \quad 1.33$$

where n is the number of points in the angular distribution and $\Delta\sigma_i(\text{exp})$ is the estimated error in the experimental values.

1.11 Ambiguities

As it turns out the parameters which yield a good fit to the data are not necessarily unique. There are several ambiguities in the optical model, the most common of which will now be briefly mentioned.

The first is the Ur^n ambiguity where n is about 2 for low energies and varies up to 3 at high energies. If Ur^n is kept constant, then r_0 can often be varied over a range of values without affecting the fit to any great extent. At low energies, this corresponds to parameters that give the same number of waves inside the nucleus. To offset this ambiguity it has become standard practice to hold the radius constant for each fit.

However, it is then possible to obtain good fits for two totally different well depths but without any radical change in the other parameters. This occurs when two different potentials have the same external wave function but different integral numbers of wavelengths inside the nucleus. This ambiguity is most important at low energies where only one partial wave contributes significantly. At higher energies several waves contribute and the ambiguity could not exist for all of them simultaneously. Another ambiguity is of the V-W type. In this case identical phase shifts can be obtained with different sets of values for V and W while the other parameters remain constant. An analysis of the scattering of strongly absorbed particles (Dr 63) has shown how these ambiguities depend on reflection from the centrifugal barrier and from the nuclear surface at various energies.

These ambiguities cannot be resolved by elastic scattering alone and one must therefore look at the nuclear reactions in order to uniquely determine the parameters.

1.12 Limitations

When working with the optical model, one should always take into consideration its various limitations. Firstly, in the low energy region the compound nucleus can exist in several sharp states and unless the energy spread of the incident beam is larger than the mean level spacing, the scattering cross-sections will show fluctuations that cannot be accounted for by an optical potential. Also as the incident energy is increased more inelastic processes become possible as their thresholds

are passed, and this produces discontinuities in the absorption cross-section and thus variations in the scattering cross-sections.

Since the optical potential yields the shape elastic cross-section and experimentally we measure both the shape elastic and the compound elastic, it is very important to obtain an estimate of the compound nucleus contribution before applying the optical model to the data.

In the region of high energy (≥ 300 MeV), the number of partial waves taking part becomes so large that numerical computations become too lengthy.

For the very light nuclei, exchange reactions can occur frequently enough to render the optical model invalid except at small scattering angles. One must also be aware of other various physical reasons why the optical model may not work for a particular set of data, for example, the elastic scattering by highly deformed nuclei or the strong coupling to a dominant inelastic channel.

1.13 Applications of the Optical Model

It has been shown by much experimental data that the optical model can give good fits to the elastic cross-sections. The optical potential is now used for the analysis of stripping data by the distorted wave Born approximation. In this type of analysis, the real potential is used as the distorting potential for the stripping interaction and the imaginary part determines how many particles are available for the interaction by absorbing them from the incident beam.

The optical model has also been successfully incorporated into low energy resonance theory (Vo 62). Furthermore in the bound-state problem, it is found that potential wells giving the observed level structure are very similar to the corresponding scattering potentials.

The radii of the optical potentials are related to the nuclear radii, and the well-known $A^{\frac{1}{3}}$ law is confirmed by the optical model analysis. There is a difference in the radius parameter when the same target nucleus is bombarded by different types of particles, ie. protons, deuterons, etc. However, this can be attributed in part to the different sizes of the incident particles.

The surface diffuseness parameter is related to the surface diffuseness of the target nucleus and it is hoped that if the information contained in the analysis of elastic scattering of different projectiles by the same nucleus could be sorted out more would be known about the nuclear surface. There is some indication in the analysis of helion scatterings that the effects of the closure of nuclear shells can be detected.

Thus the phenomenological optical potential is useful in nuclear studies but what is really needed is a theory to explain the interactions that take place during the scattering or absorption of the incident particle. Such a theory is essentially a many-body one and will therefore be quite complex.

CHAPTER 2

EXPERIMENTAL

2.1 Scattering Chamber

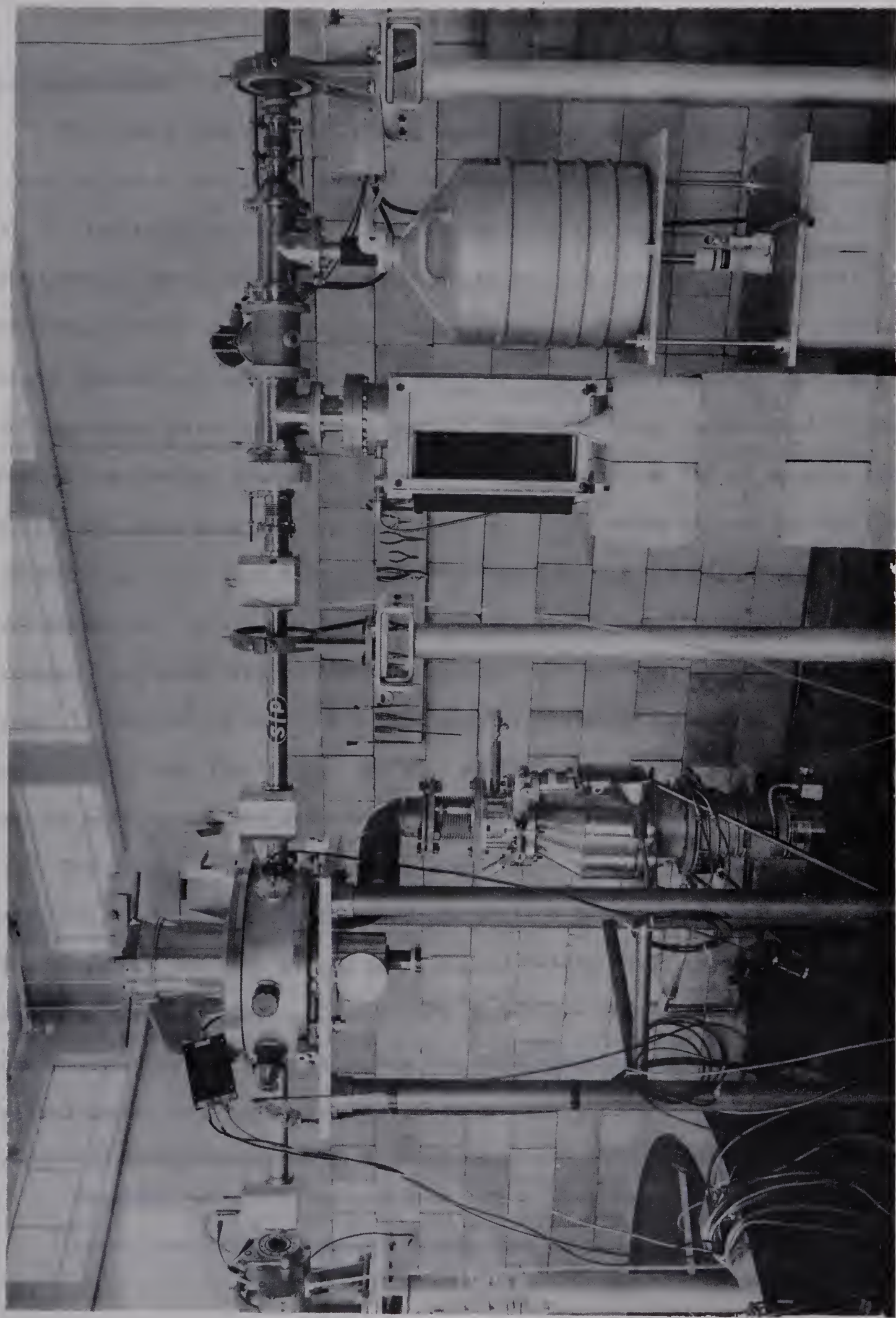
All of the angular distributions for this experiment were obtained using the University of Alberta C.N. Van de Graaff[†] and a charged particle scattering chamber. The scattering chamber was designed by G. Roy with the technical assistance of N. Riebeek and was installed just before this project was undertaken. As this will be the first time that this system is described, the apparatus will be discussed in some detail.

As can be seen in the photograph in fig. 2.1 the beam, after 90° magnet analysis, passes through a 'cold finger', a beam profile monitor, the slit system, the scattering chamber and is finally stopped by a Faraday cup.

A full description of the slit system is given elsewhere (Ro 69). Briefly the slits are made of tantalum and are independently adjustable in the vertical and horizontal position. Thus by careful alignment of the two slits and with the aid of an antiscattering slit at the entrance to the chamber it is possible to eliminate most of the background originating from the slit system. Typically for 3 MeV protons less than 100 multiple scattering events have been observed for an integrated charge of 1,000

[†]High Voltage Engineering Corp., Burlington, Massachusetts.

Figure 2.1 The charged particle system.



microcoulombs.

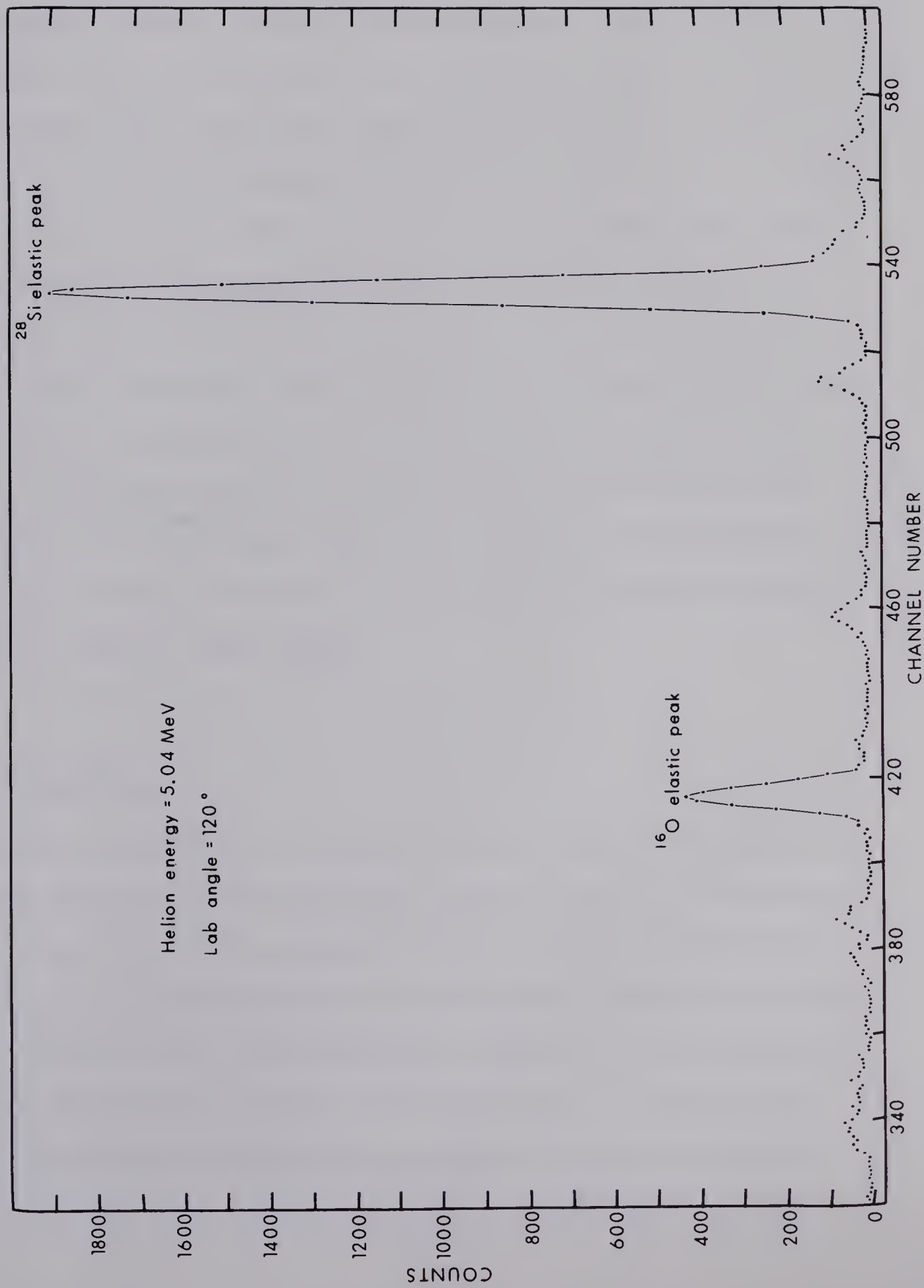
The scattering chamber is 18 inches in diameter and contains a rotating plate into which solid state detector holders can be positioned at 10° intervals and either 4 or 8 inches from the target. On the side of the chamber there are 6 openings of which two are used as viewing ports, and the others hold a thermocouple vacuum gauge, an ion vacuum gauge, a solid state detector at 90° to the beam axis for monitoring purposes, and a high voltage input for biasing the targets. The Faraday cup is situated 18 inches behind the chamber and has a suppressor ring mounted on teflon spacers approximately $1/2$ inch from the cup and biased at -1,000 volts to prevent the loss of electrons. Up to 4 targets can be mounted in the chamber at one time and any one may be brought into the beam and rotated to the reflection or transmission mode without breaking vacuum. A 6 inch mercury diffusion pump[†] is mounted on the base of the chamber and with the aid of an ion pump on the beam line before the slit system pressures of about 1×10^{-6} mm of mercury or less are easily maintained in the system.

The detectors presently being used in the chamber are 10 mm in diameter, 1,000 micron depletion depth silicon detectors from Ortec^{††}. The detectors are each placed in a special holder which is then mounted onto the rotating plate. Collimators of various lengths and diameters can be used with each detector but for this experiment, the collimators were 3 inches long with openings of about $3/16$ inches in diameter. The

[†]Edwards, 430 South Service Road, West, Oakville, Ontario.

^{††}Ortec, Oak Ridge Technical Enterprises Corp., Oak Ridge, Tennessee.

Figure 2.2 A typical spectrum for helions on a self-supporting SiO target.



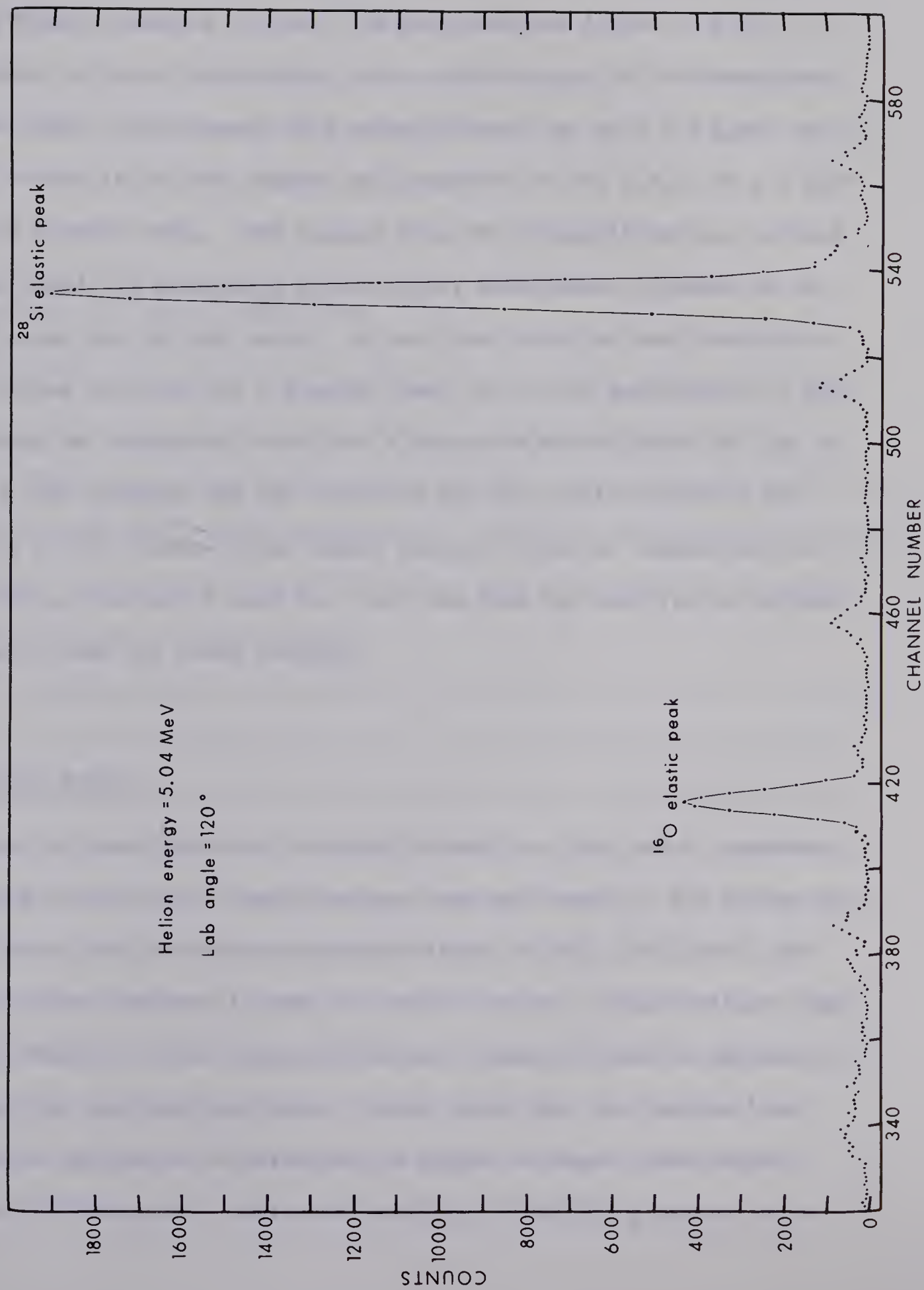


plate on which the detectors are mounted can be rotated from outside the chamber without breaking vacuum. The detectors are joined to B.N.C. connectors, on top of the chamber, via a short length of low capacitance shielded cable. Ortec model 109A preamplifiers, set at a 1 x gain, are mounted on the lid of the chamber and connected to the B.N.C. by a 3 inch length of coaxial cable. The signals from the preamplifiers are carried to Ortec model 440 selectable active filter amplifiers, situated in the control room, via 100 ohm cable. It was found that the best resolution, 20-25 keV, was obtained for a shaping time, set on the amplifier, of 1 μ sec.

During an experiment, data from 4 detectors are collected on line by an S.D.S. 920 computer and the data from the 90° monitor detector are stored by a 1024 channel pulse height analyzer which is dumped into the S.D.S. 920 at the end of each run. All the data for each run is written on magnetic tape for later analysis.

2.2 Target Biased

With the installation of a target biased by G. Roy and W. Saunders, the taking of excitation curve data was made much easier. For taking this type of data, the detectors are usually placed at 60°, 120°, 140°, 160° and the monitor detector is used for the 90° point. A high voltage supply is then connected to the target holder and a positive bias is applied to slow down the incident particles. It was found that the maximum bias that can be applied is 50 kilovolts, as higher voltages cause excess noise in the detectors. Thus after setting the analyzing magnet for a

particular beam energy one can obtain an excitation curve, in as fine divisions as necessary, over a 50 kilovolt interval before the analyzing magnet has to be readjusted along with the beam conditions. The whole procedure for taking excitation curves has thus been simplified and speeded up.

2.3 Targets and Target Preparation

For good resolution on the charged particle system target thicknesses of $50 \mu\text{gm}/\text{cm}^2$ or less were found necessary. Further in order to have as few contaminant peaks as possible it is desirable to have pure self-supporting targets whenever this can be accomplished. Therefore, self-supporting targets of aluminum (Al) and silicon monoxide (SiO) were made along with a sodium fluoride (NaF) on a formvar backing.

The aluminum target was prepared by evaporating thin strips of aluminum foil from a coil of tungsten wire, onto a glass slide which had previously been coated with an evaporated layer of salt (NaCl). The aluminum coating was then floated off in water and the foil was picked up on a target blank. It was found that if an aluminum target was thin enough to see through when held up to a light then a good spectrum could be obtained from it.

The SiO target was prepared by evaporating a weighed amount of SiO, from a molybdenum boat, onto a salted glass slide. The SiO was then floated off the slide and picked up on a target blank.

A NaF target was made by evaporating NaF onto a target blank with a formvar backing.

Formvar[†] backings are prepared by first dissolving 2% by weight of Formvar 15/95E powder in 1, 2 Dichlorethane. When a drop of this solution is placed on water, it spreads out to form a thin film which can then be picked up by a target blank.

The target blanks consisted of a 1/2" x 1" piece of thin aluminum with a 1/2" hole in the center.

2.4 Relative Cross-Section Measurements

The relative cross-sections for the elastic scattering angular distributions were normalized to a monitor detector situated at 90°. Normalizing to a monitor detector instead of the integrated beam current, collected in the Faraday cup, automatically corrected for target inhomogeneities which would be noticeable if the beam spot wandered slightly or if the target angle was not set accurately.

The relative solid angle for the detectors was determined by setting each detector at 90° and comparing the counts for a particular peak.

Data points between 30° and 100° for each angular distribution were obtained with the target at 35° to the incident beam and in transmission mode. For the cross-section measurements from 90° to 160°, the target was rotated through 90° into the reflection mode.

The relative cross-section could not be measured further forward than 30° because of the dead time limitations and also the various elastic

[†] Shawinigan Resins Corp., Springfield, Massachusetts.

peaks overlapped too much to allow the extraction of peak areas.

Each angle was run until there were at least 9,000 counts in the elastic peak. The statistical error was, therefore, less than 1.1%. However, in the forward angles the major error is caused by the setting of the detector angle. At the present time, the detector angle cannot be set more accurately than to about $\pm 0.2^\circ$. Because of the rapid drop off in the angular distribution in the forward angles this can introduce an error of about 8% which is very noticeable in the values of σ/σ_R , the ratio of the elastic to Rutherford cross-sections.

2.5 Absolute Cross-Sections

After the relative cross-section measurements were made, the target was left in the transmission mode with the detectors at 30° , 40° , 50° and 60° , and a low energy (~ 2 MeV) proton beam was run on the target. According to optical model calculations, this scattering is greater than 95% Rutherford back to 80° for most of the nuclei studied. Therefore, by comparing the number of counts accumulated, for a specified total charge, with the known Rutherford cross-section, it is possible to obtain a conversion factor to determine the absolute cross-sections from the relative cross-sections.

The absolute cross-sections for the 5.0 MeV data were obtained in this manner but because of the voltage conditioning necessary to run the Van de Graaff at 6.5 MeV, it was not possible to bring the energy of the machine down for this data. Therefore, an estimate of the absolute cross-sections

for the 6.5 MeV data was obtained by doing optical model calculations with parameters reported for neighbouring nuclei or ones reported for the same nuclei but different energies. The results obtained from several sets of parameters indicated a consistency in the angles forward of 50° to within 10%. Thus a reasonable estimate for the absolute cross-sections the 6.5 MeV data was obtained.

2.6 Data Reduction

As mentioned previously, the spectra from each of the four detectors along with the monitor spectrum were recorded on magnetic tape for future analysis. In addition, the total integrated charge collected in the Faraday cup, the true time, the live times for each detector and the angles of the detectors were recorded.

The first step in the data reduction was to extract the areas of the elastic peaks from the spectra. The spectra were first plotted out by the University of Alberta IBM 360 by means of a plot and print program written at this laboratory (Da 69b). The program incorporates the background subtraction routines used in the program Tepel (Te 66). This is the most tedious part of the analysis since the spectra contain the peaks from all the charged particle reactions that occurred and one must not only subtract background but also try and extract various contaminant peaks which overlap the elastic peaks. In addition to the peaks caused by helium induced reactions on the target nucleus, there are always contaminants on the target, notably carbon and oxygen, which will interfere with

the peak of interest. This is especially true in the forward angles where overlap of the various elastic peaks restricts obtaining data forward of 30° and usually limits one to 35° .

Once the peak areas were determined, this information along with the dead time, monitor, solid angle, and absolute cross-section normalization factors were used to determine the absolute cross-sections. The normalization calculations were carried out with an APL (Fa 68) program via a remote terminal connected to the IBM 360. As this terminal was on line with the computer, any errors in determining the angular distributions could be detected and corrected immediately. The APL program calculated the absolute cross-sections for both the laboratory and center of mass coordinate systems, the center of mass angles and σ/σ_R the ratio of the elastic to the Rutherford cross-section. This information was then punched up on cards for use with the optical model fitting program.

In contrast to charged particle work done with a magnet (Gu 68), it is very easy to collect data with a scattering chamber. However, the fact that so much information is collected makes the data reduction more difficult. A rule of thumb is that of all the peaks in a spectrum, the one of interest will be most seriously affected by contaminant peaks.

CHAPTER 3

ANALYSIS AND RESULTS

3.1 Compound Nucleus Contribution

Since the optical model calculates the shape elastic scattering only and experimentally the shape elastic plus the compound elastic scattering are measured, it is very important to obtain an estimate of the compound nucleus contribution before attempting to fit the experimental data with the optical model. A program to do Hauser-Feshbach calculations (Sm 67) and modified by N. Davison (Da 69a) to include level density formulae was used for this purpose.

The calculations indicated that the compound elastic cross-section was at most 0.04 mb/sr and typically 0.02 mb/sr. Since the smallest cross-section measured was ~3.4 mb/sr, for the back angles of the 6.5 MeV ^{19}F angular distribution, it can be concluded that the scattering is primarily shape elastic with the compound elastic contribution being less than 1.2%. No increase in this estimate was obtained by making alterations in the parameters used for the calculations.

There are several possible explanations as to why the compound contribution is so small for these four nuclei. Since the Coulomb barriers for helions on these nuclei are of the order of 6.0 MeV, the probability of penetrating into the nucleus is fairly small for the bombarding energies used. Furthermore there are many helion induced

Table 3.1

Level Density Parameters for Hauser-Feshbach Calculations

$$\log_{10} N(E_x) = a + b \sqrt{E_x}$$

Nucleus	a	b
^{18}F	- 0.108	0.637
^{19}F	- 0.480	0.670
^{20}Ne	- 1.128	0.750
^{21}Ne	- 0.768	0.720
^{21}Na	- 0.480	0.704
^{22}Na	- 0.305	0.763
^{23}Na	- 1.15	1.00
^{25}Mg	- 0.592	0.833
^{25}Al	- 0.005	0.538
^{26}Al	- 0.442	0.885
^{27}Al	- 0.960	0.960
^{27}Si	- 0.765	0.869
^{28}Si	- 1.65	0.957
^{29}Si	- 1.46	1.11
^{29}P	- 0.820	0.810
^{30}P	- 0.690	0.885

reactions energetically possible at 5.0 MeV and higher, with most having Q values of 2 MeV or more. Therefore, once the compound nucleus is formed there are many possible exit channels competing with the compound elastic channel and its cross-section will be decreased accordingly.

Since the compilation of the input data for the Hauser-Feshbach program is a lengthy process, especially the level density parameters, this information has been tabulated. If $N(E_x)$ represents the number of levels below an excitation energy E_x , then the level density is found to approximately follow the relationship $\log_{10} N(E_x) = a + b\sqrt{E_x}$. The slope and intercept of this line are found by plotting $\log_{10} N(E_x)$ vs $\sqrt{E_x}$ for each nucleus used in the program.

3.2 Excitation Curves

The optical model, as discussed in the first chapter, is not capable of describing the fine resonance structure that can be observed at low energies. Therefore, it is necessary to ascertain whether or not the energy spectrum exhibits any fluctuations in the region where the angular distribution is to be taken.

Because of technical difficulties, it was not possible to operate the accelerator in the 6 MeV region after the first measurements had been taken at 6.5 MeV. Therefore, excitation curves for the 6.5 MeV angular distributions were not obtained and as a result, the optical model parameters determined for these data are subject to the possibility that resonance fluctuations may exist in that region.

Figure 3.1 Excitation curves for ^{19}F taken at 60° , 90° , 120° , 140° and 160° . The statistical errors are about 5%.

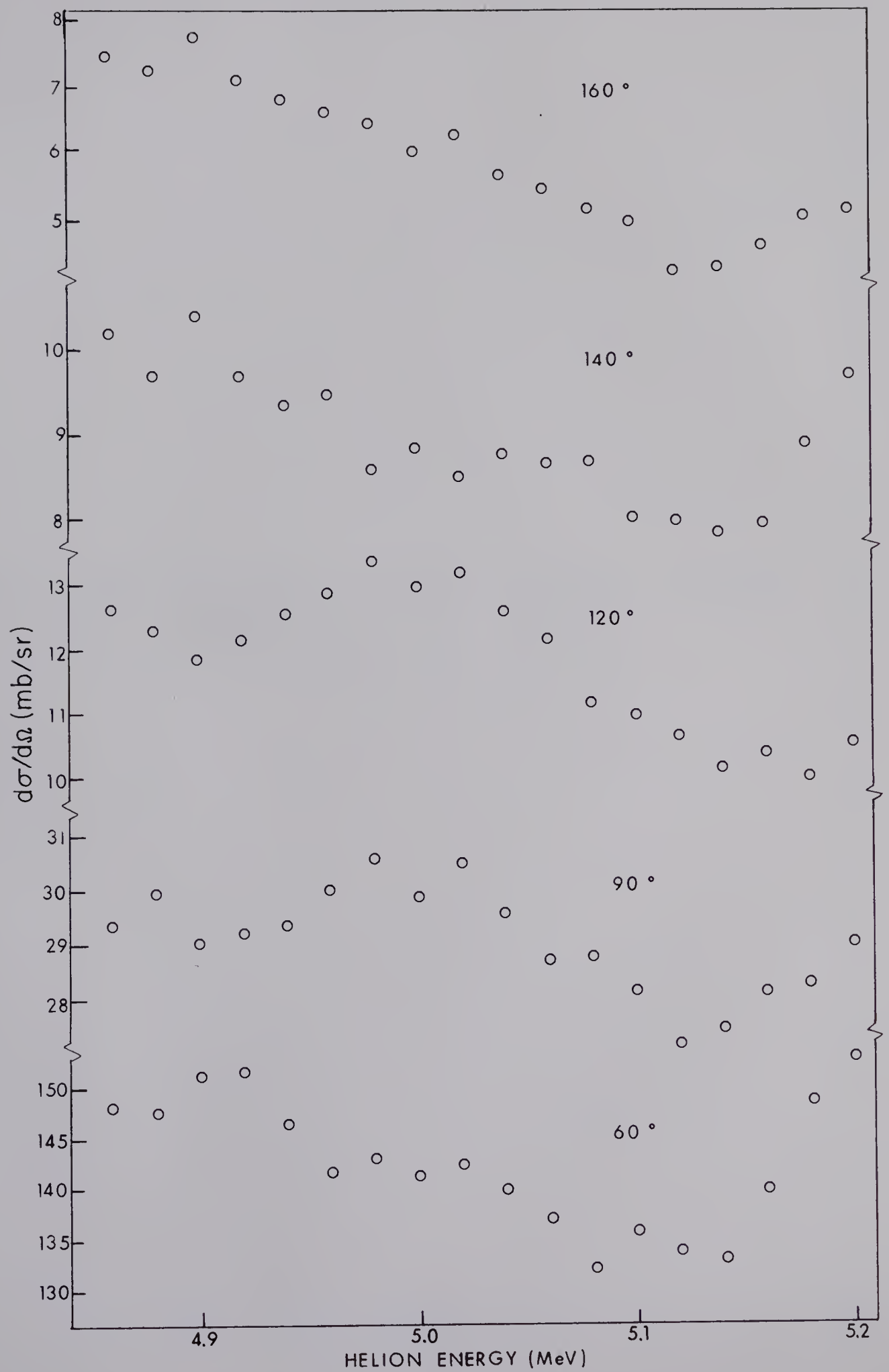


Figure 3.2 Excitation curves for ^{23}Na taken at 60° , 90° , 120° , 140° and 160° . The statistical errors are about 5%.

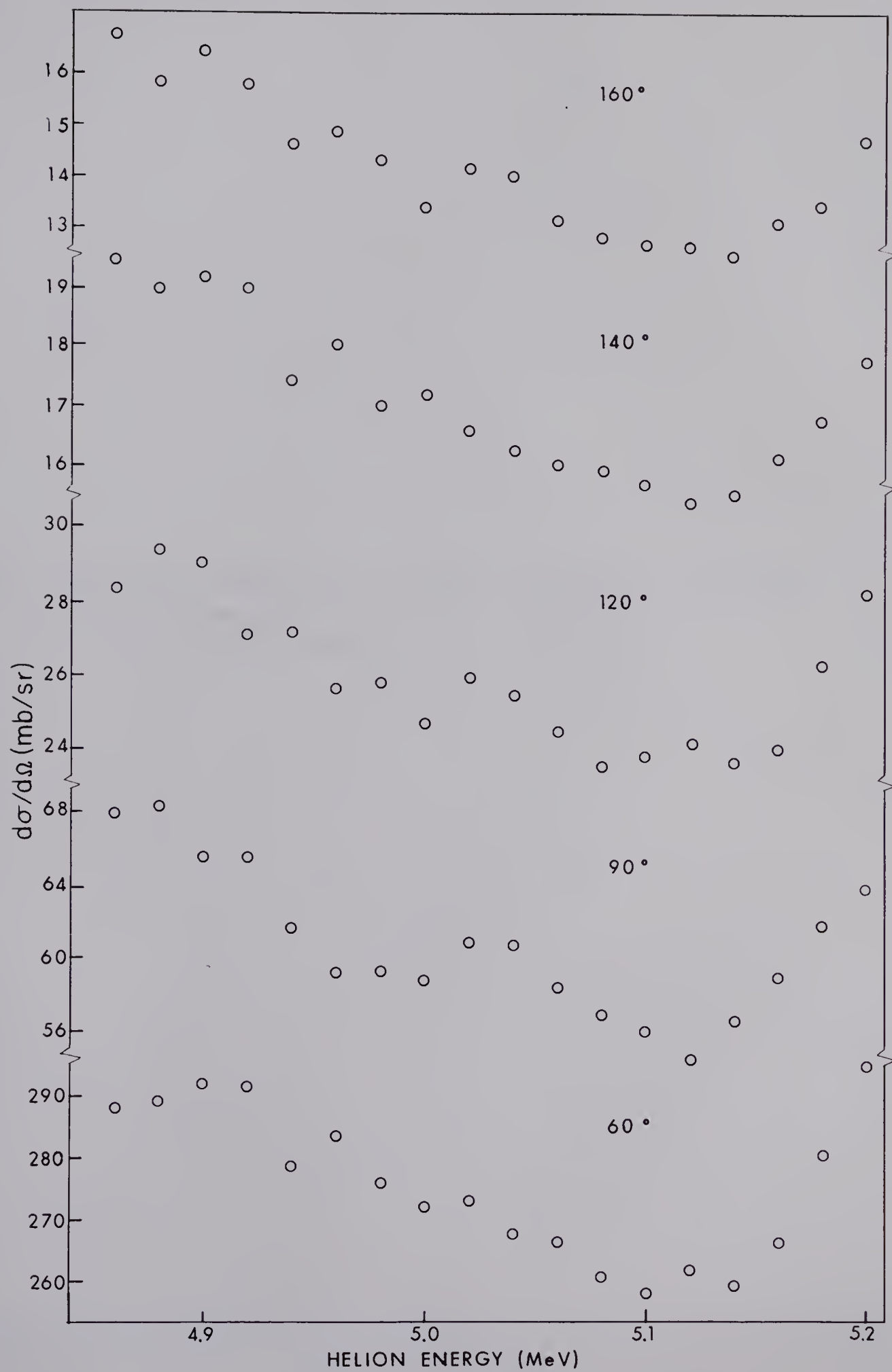


Figure 3.3 Excitation curves for ^{27}Al taken at 60° , 90° , 120° , 140° and 160° . The statistical errors are about 5%.

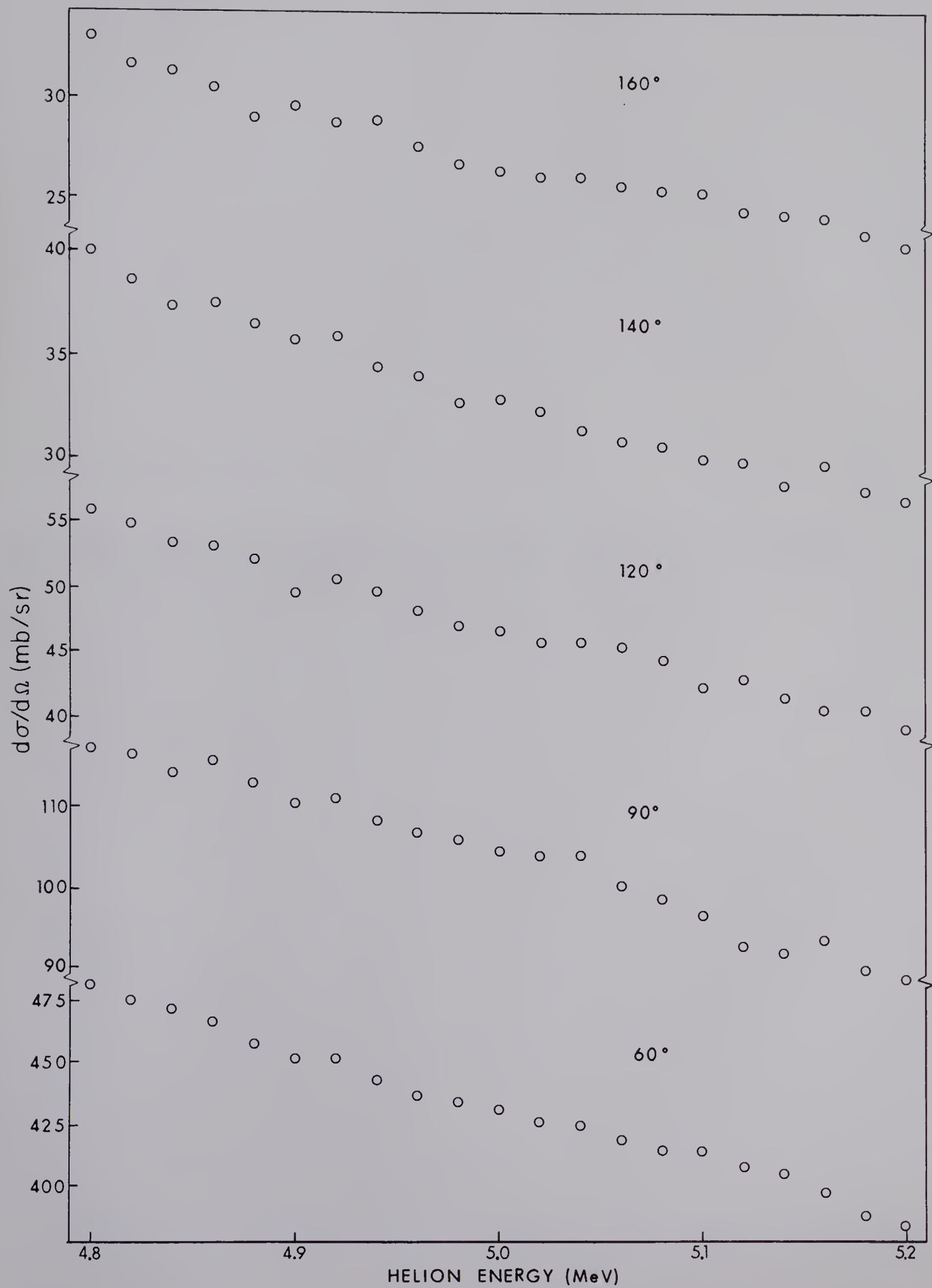
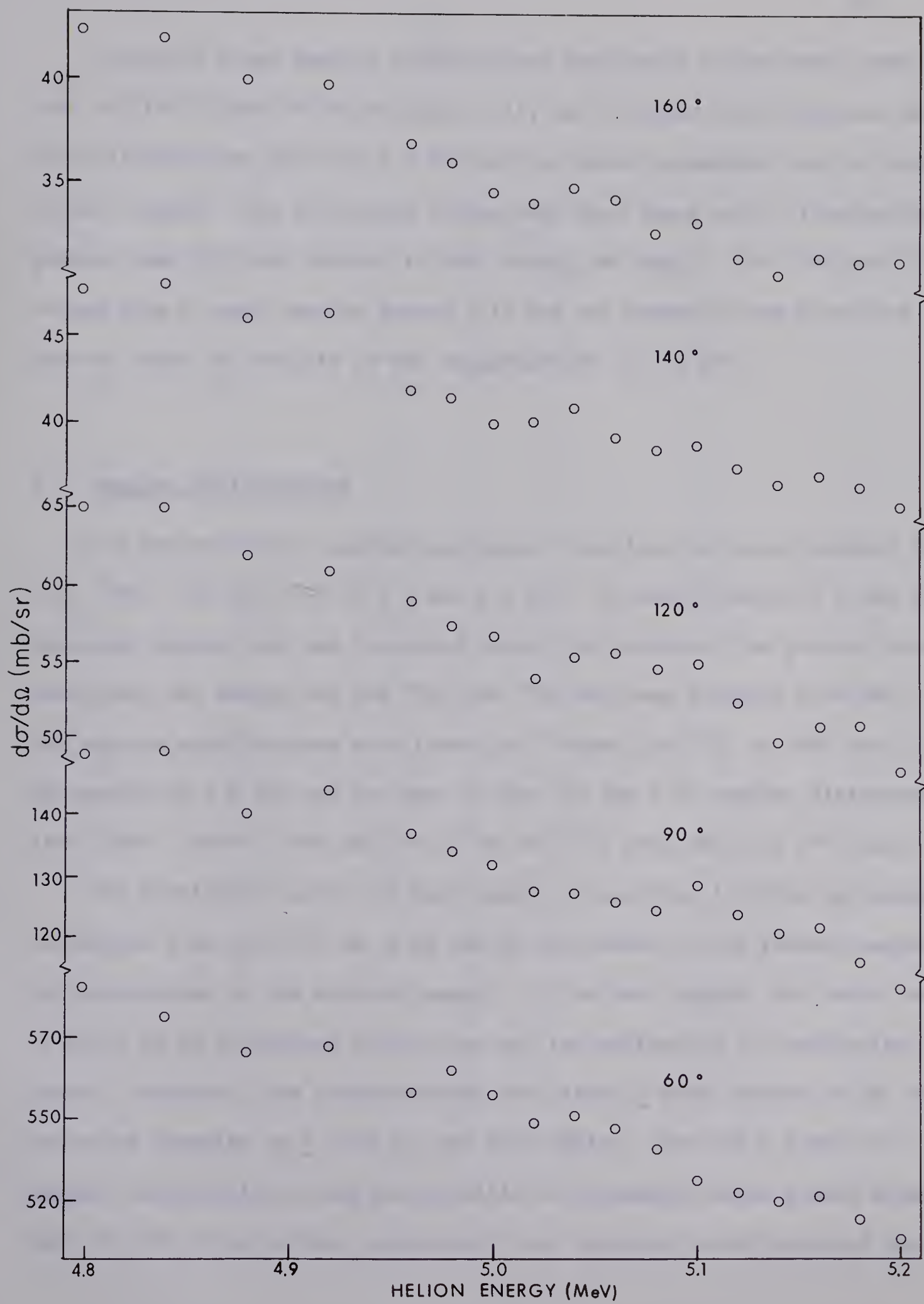


Figure 3.4 Excitation curves for ^{28}Si taken at 60° , 90° , 120° , 140° and 160° . The statistical errors are about 5%.



For the 5.0 MeV angular distributions excitation curves were taken from 4.8 to 5.2 MeV in 20 keV steps. If, as it turned out, there are no large fluctuations then the 5.0 MeV optical model parameters can be trusted in this region. The excitation curves show that there are no fluctuations greater than 10% with respect to both energy and angle. The ^{23}Na and ^{19}F curves show a trend upwards beyond 5.14 MeV but generally one should be able to trust the results in the neighbourhood of 5.0 MeV.

3.3 Angular Distributions

The helion elastic scattering angular distributions were obtained for ^{19}F , ^{23}Na , ^{27}Al and ^{28}Si at 5.0 and 6.5 MeV. A recalibration of a new 90° analyzing magnet that was installed during the course of the project indicated that the energy for the ^{27}Al and ^{28}Si data was actually 5.04 MeV. The angular distributions were taken in 5° steps from 30° to 160° for all the nuclei at 5.0 MeV and for part of the ^{19}F and ^{27}Al angular distributions at 6.5 MeV. The 6.5 MeV data for ^{23}Na and ^{28}Si were taken in 10° steps.

The statistical error for each point is less than 1.1% but as mentioned in chapter 2 an error of up to 8% can be introduced in the forward angles by inaccuracies in the detector angle. In the back angles, the major source of error is in background subtraction and the extraction of overlapping peaks. Therefore, the cross-sections are within $\pm 6-8\%$ forward of 50° with the error dropping to $\pm 3-5\%$ for the back angles. For the 5.0 MeV ^{19}F angular distribution it was not possible to accurately extract peak areas back of 120° since so many contaminant (ie. reaction) peaks appeared that

Table 3.2

 $^{19}\text{F}(^3\text{He}, ^3\text{He})^{19}\text{F}$ - Elastic Scattering Cross-Sections

5.0 MeV			6.5 MeV		
c.m. Angle	σ mb/sr	σ/σ_R	c.m. Angle	σ mb/sr	σ/σ_R
40.2	1421	0.881	28.9	2791	0.805
45.9	839	0.857	34.6	1355	0.790
51.5	499	0.785	40.2	687	0.720
57.0	319	0.733	45.9	367	0.634
62.5	203	0.651	51.5	205	0.544
67.9	141	0.608	62.5	91.5	0.496
73.3	101	0.568	67.9	68.2	0.475
78.6	74.2	0.529	73.3	49.0	0.466
83.8	57.8	0.510	78.6	35.1	0.423
89.0	45.3	0.485	83.8	27.0	0.403
94.1	38.1	0.485	89.0	21.4	0.388
99.2	30.2	0.450	94.1	16.5	0.355
104.1	25.0	0.428	99.2	13.7	0.344
109.0	21.9	0.427	109.0	9.72	0.320
113.8	19.4	0.423	113.8	7.92	0.292
118.6	16.9	0.409	118.6	6.66	0.272
123.3	15.3	0.406	123.3	6.27	0.282
			127.9	5.57	0.272
			132.5	4.73	0.249
			137.0	4.30	0.242
			145.9	3.75	0.235
			150.2	3.72	0.243
			154.6	3.50	0.238
			158.9	3.59	0.252
			163.1	3.38	0.242

Table 3.3

 $^{23}\text{Na}(^3\text{He}, ^3\text{He})^{23}\text{Na}$ - Elastic Scattering Cross-Sections

5.0 MeV			6.5 MeV		
c.m. Angle	σ mb/sr	σ/σ_R	c.m. Angle	σ mb/sr	σ/σ_R
39.3	2508	1.001	33.8	2404	0.900
44.8	1497	0.986	44.9	639	0.711
50.3	867	0.883	55.8	228	0.574
55.8	583	0.869	66.5	98.9	0.471
61.2	379	0.792	77.1	54.9	0.436
66.5	272	0.768	87.4	34.0	0.408
71.8	196	0.723	97.6	22.0	0.371
77.1	146	0.687	107.4	13.5	0.300
82.3	114	0.663	117.1	9.47	0.264
87.4	89.2	0.633	126.5	5.97	0.200
92.5	72.3	0.613	135.8	5.28	0.205
97.6	58.9	0.587	144.8	4.04	0.176
102.5	51.1	0.589	153.8	4.04	0.191
107.4	44.7	0.587	162.6	4.02	0.202
112.3	37.2	0.552			
117.1	33.0	0.544			
121.8	29.0	0.526			
126.5	25.4	0.503			
131.2	22.8	0.487			
135.8	20.7	0.475			
140.3	18.9	0.460			
144.8	16.9	0.435			
149.3	15.9	0.429			
153.8	14.7	0.412			
158.2	14.5	0.421			
162.6	13.7	0.407			
167.0	13.3	0.402			
171.3	13.0	0.399			

Table 3.4

 $^{27}\text{Al}(^3\text{He}, ^3\text{He})^{27}\text{Al}$ - Elastic Scattering Cross-Sections

5.04 MeV			6.5 MeV		
c.m. Angle	σ mb/sr	σ/σ_R	c.m. Angle	σ mb/sr	σ/σ_R
33.2	6459	1.010	44.1	1159	0.900
44.1	2120	0.990	49.5	665	0.800
49.5	1328	0.960	54.9	421	0.743
54.9	849	0.901	60.3	286	0.708
60.3	613	0.912	65.6	195	0.655
65.6	424	0.855	70.8	140	0.614
70.8	320	0.845	81.2	83.0	0.581
76.0	245	0.826	86.3	65.4	0.558
81.2	190	0.797	91.4	52.4	0.536
86.3	153	0.785	96.4	41.0	0.494
91.4	126	0.778	101.4	33.6	0.469
96.4	104	0.754	106.3	28.3	0.453
101.4	85.3	0.718	111.2	22.5	0.406
106.3	74.9	0.720	116.0	19.6	0.396
111.2	64.3	0.699	120.8	17.5	0.390
116.0	57.0	0.692	125.6	15.2	0.371
120.8	48.8	0.655	130.3	12.8	0.338
125.6	45.1	0.661	134.9	10.9	0.310
130.3	39.5	0.627	139.5	11.2	0.337
134.9	36.7	0.626	144.1	10.2	0.325
139.5	33.4	0.607	148.7	9.83	0.329
144.1	31.2	0.599	153.2	9.44	0.330
148.7	29.6	0.597	157.7	9.35	0.338
153.2	28.2	0.592	162.2	8.63	0.321
157.7	27.6	0.601			
162.2	26.2	0.585			
166.7	25.1	0.573			
171.1	24.8	0.575			

Table 3.5

$^{28}\text{Si}(^3\text{He}, ^3\text{He})^{28}\text{Si}$ - Elastic Scattering Cross-Sections

5.04 MeV			6.5 MeV		
c.m. Angle	σ mb/sr	σ/σ_R	c.m. Angle	σ mb/sr	σ/σ_R
38.6	4098	0.991	33.1	4495	1.000
49.4	1606	0.995	44.0	1439	0.938
54.7	1055	0.960	54.8	576	0.876
60.1	738	0.943	65.4	267	0.759
65.4	549	0.950	75.8	141	0.703
70.6	406	0.923	86.1	84.9	0.617
75.8	304	0.883	96.2	55.3	0.578
81.0	240	0.870	106.1	38.1	0.515
86.1	189	0.836	115.8	27.2	0.486
91.2	155	0.822	125.4	20.3	0.416
96.2	126	0.785	134.7	15.9	0.400
101.2	106	0.771	144.0	13.3	0.347
106.1	88.6	0.736	153.1	11.7	0.363
111.0	78.3	0.736			
115.8	67.5	0.709			
120.6	60.3	0.700			
125.4	55.3	0.702			
130.1	51.0	0.702			
134.7	46.5	0.687			
139.4	43.8	0.690			
144.0	41.2	0.685			
148.6	38.7	0.677			
153.1	37.8	0.689			
157.6	36.0	0.679			
162.1	34.6	0.672			
166.6	34.0	0.674			
171.1	33.6	0.677			

the helion elastic peak was obliterated. These peaks grew larger than the elastic peak for the back angles and overlap was so bad that proper peak identification was not possible. It is thought that most of the contaminant peaks were from ($^3\text{He},p$) reactions from ^{19}F and ^{12}C .

The helion Coulomb barrier for these four nuclei is about 6.0 MeV and thus the helion particle is unable to penetrate the nucleus to any great extent and as a consequence, the angular distributions show very little structure. Therefore, one must be careful when fitting with the optical model as the data may be over parameterized.

3.4 Fitting Procedure

In keeping with recent optical model analysis for helions (Ab 66) and deuterons (Pe 67), the real well depth was expected to be in the vicinity of the sum of the constituent nucleon potentials. Therefore, during the searches the real well depth was confined in the region between 100 and 200 MeV. Earlier investigations for helion elastic scattering gave well depths of about 50 MeV but subsequent use of these optical model potentials for the study of helion induced reactions indicated that a deeper well was preferred.

For this work the fits were initially attempted with a surface-peaked derivative Saxon-Woods form for the imaginary potential. However, it was found and has been previously shown (Ho 61a) that the analysis of helion elastic scattering is insensitive to the form chosen for the imaginary potential. It is now customary to use a standard Saxon-Woods form

and the fitting was therefore carried out with this type of imaginary potential. The reason for this insensitivity is that the helion particle is either scattered or absorbed in the region of the nuclear surface and thus is not affected by the potential in the interior since it will probably not penetrate there.

A spin-orbit potential was not used in this analysis for several reasons. First, there is still very little data available on the polarization of elastically scattered helions. Present data indicates a spin-orbit potential of about 3.0 MeV (Ba 67a) but values as high as 8.0 MeV (Pa 68) have been used. Secondly, the introduction of extra parameters will necessarily improve the fit and due to the nature of the angular distributions one would not be able to definitely attribute any improvement to the inclusion of a spin-orbit term.

The optical model potential used was of the form

$$V(r) = V_C(r) - Uf(r) - iWg(r) \quad 3.1$$

where $V_C(r)$ is the Coulomb potential of a uniformly charged sphere (see eq. 1.25), U and W are the real and imaginary potential depths and $f(r)$ and $g(r)$ their form factors. For this analysis, the Saxon-Woods form factor

$$f(r) = g(r) = \frac{1}{1 + \exp\left(\frac{r-r_0}{a_0} A^{\frac{1}{3}}\right)} \quad 3.2$$

was used. The angular distributions were fitted using an optical model code of Perey. The Coulomb radius parameter, r_C , was held fixed at 1.4 fm

which is a standard value for helion optical model analysis. This value is not critical for good fits to the data.

The first searches were three parameter attempts where the real and imaginary radii, r_u and r_w , were set equal as were the real and imaginary diffuseness, a_u and a_w . The real well depth was stepped in 10 MeV increments from 100 to 200 MeV while searches on r , a and W were carried out. The fits thus obtained were not satisfactory so the constraint on the radii was released and four parameter searches were attempted. This gave some improvement but it appeared that the real and imaginary radius and diffuseness parameters could not be set equal. This meant five parameter searches, over r_u , r_w , a_u , a_w and W , had to be carried out. With five free parameters, the χ^2 space is filled with local minima which could trap the search routine and one must therefore apply some constraints to the parameters.

There are two possibilities available for constraining the parameters. One is to step over two or three of the parameters, in addition to the real well depth, while searching the others. To do this effectively requires a considerable amount of computer time. The other possibility is to fix one or more of the parameters to some average value while adjusting the rest for a good fit. In a recent survey (Ho 68) of helion elastic scattering data, it is shown that the real radius can be held at about 1.07 or 1.14 fm. Therefore, throughout the analysis, the real radius was allowed only these values. This constraint was released once good fits were obtained to determine if any variation in the radius occurred.

With the radius thus fixed, the procedure was to step over the real potential in 10 MeV increments from 100 to 200 MeV, the imaginary potential

in 1 and 3 MeV increments from 6 to 27 MeV and the imaginary diffuseness in 0.05 fm increments from 0.60 to 0.95 fm. It was found that one could simultaneously step and search the real potential without serious difficulties.

There were some problems in searching the imaginary parameters. If all three imaginary potential parameters (r_u , a_w , W) were released the searches yielded unreasonable values. Typically the imaginary well depth would become small, ~ 3 MeV, and either the imaginary radius or diffuseness or in some cases, both would become quite large, $r_w \sim 2.4$ fm and $a_w \sim 2.0$ fm. As it turned out a unique set of parameters for each angular distribution could not be found. Therefore, several sets of parameters have been tabulated for each nucleus.

3.5 Results and Conclusions

Generally the results are typical of the helion optical model parameters as found by other studies. The real well depths are in the vicinity of 150 MeV but shallower and deeper wells were also found which can probably be attributed to one or more of the ambiguities. The real radius and diffuseness parameters lie within the range of values established by others, that is, $r_u \sim 1.1$ fm and $a_u \sim 0.78$ fm. Therefore, the real part of the optical model potential is seen to satisfactorily represent these data.

The imaginary potential parameters, however, reveal several interesting features. The most notable is that in all cases, the imaginary potential

extends beyond the real one. This confirms the idea that the helion interacts in the surface region of the target nucleus and that there is a high probability of stripping and pick-up reactions occurring there.

The imaginary potentials are found to be quite shallow, being substantially less than the sum of the constituent nucleon potentials. This result is not unique to this study and if one examines the literature, it becomes apparent that there is quite a variation in the imaginary well depths found by others.

Fluorine

The ^{19}F optical model parameters indicate a deeper imaginary potential at 6.5 MeV than at 5.0 MeV. This implies that the helion is getting closer to the target nucleus at higher energies and thus has greater probability of being absorbed and as a result, the reaction cross-section is larger at 6.5 MeV. Previous work on this nucleus was done at 6.0 MeV and higher (Ma 66) and those results agree in magnitude with the 6.5 MeV parameters found here.

Sodium

The parameters found for ^{23}Na have the same features as those for ^{19}F , ie. deeper imaginary well for 6.5 MeV. At 6.5 MeV, a good fit was obtained for a set of parameters in which the imaginary well depth and radius and real radius are relatively small while the imaginary diffuseness is fairly large. The resultant reaction cross-section is much larger than for the other parameter sets. Although these parameters are

not as 'pleasing' as the others, they cannot be ignored because of the phenomenological nature of the optical model. Previous work on ^{23}Na was done at 25.7 MeV (Go 64).

Aluminum

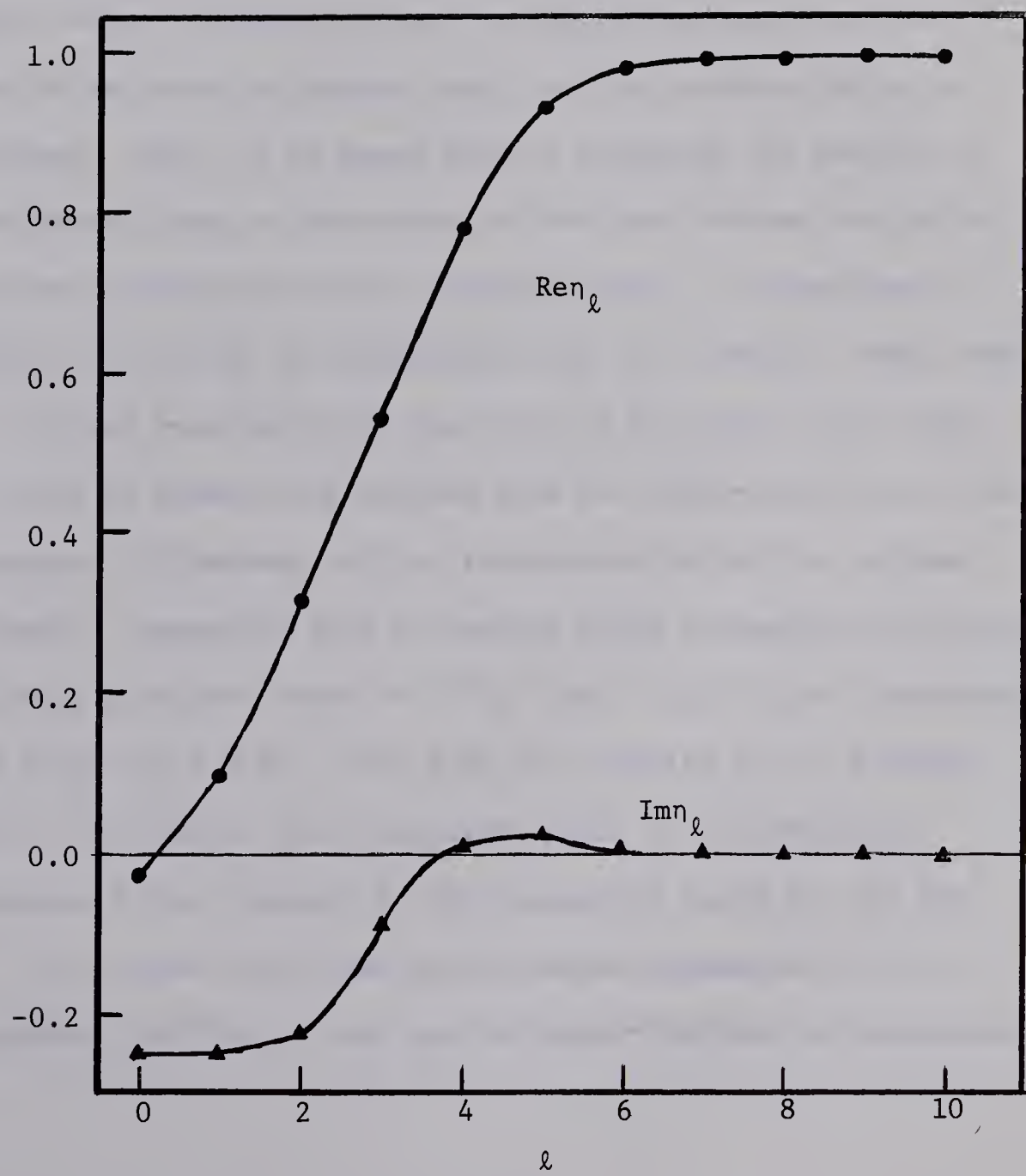
Fitting the ^{27}Al data posed some problems as at 5.04 MeV, the real diffuseness parameter had a tendency to be small and the imaginary diffuseness was large. An attempt was made to force these parameters to more 'reasonable' values without success. Previous low energy helion scattering on ^{27}Al was done at 5.5 MeV (Br 65, Ho 61b). These analyses used shallow real potentials but in the cases where deeper wells were tried, the diffuseness parameters exhibited the same effects. The 6.5 MeV results appear satisfactory.

Silicon

The ^{28}Si data at 5.04 MeV could not be properly fitted with a reasonable imaginary potential. The tendency here was towards a shallow well depth and a large radius and/or diffuseness. Attempts to constrain the parameters were unsuccessful. Since ^{28}Si does exhibit rotational levels, there is a possibility of inelastic scattering, by Coulomb excitation, which would account for the large imaginary radius. However, it is not obvious why this should only be noticeable at 5.04 MeV and not 6.5 MeV. Previous work on ^{28}Si was done at 10.0 MeV and higher (Ba 67b, Sw 67, Wi 67) so a comparison is not possible.

One must remember, when doing optical model analysis, that this is a

Figure 3.5 Plot of real and imaginary phase shifts vs ℓ for the elastic scattering of helions at 6.5 MeV on ^{19}F .



phenomenological model and therefore, parameters that intuitively seem unreasonable cannot be legitimately disregarded. Originally it was thought that the optical model analysis of helion elastic scattering would yield information about the nuclear surface. This aspiration, however, was not realized and it is now thought that this information can be gained by studying helion induced reactions below the Coulomb barrier where the incident particle is known to interact only with the surface region of the target nucleus. Also, it is hoped that by comparing the results of scattering different types of particles off the same nucleus one may be able to determine something about the nuclear surface. A comparison of the phase shifts for helions and alpha-particles, for example, shows that the range of ℓ values over which the real part of the phase shift rises from zero to unity is greater for helions than for alpha-particles. This indicates a greater diffuseness for the interaction radius for helions.

In conclusion, reasonable sets of optical model parameters for helion elastic scattering have been found for ^{19}F , ^{23}Na , ^{27}Al , ^{28}Si at bombarding energies of 5.0 MeV and 6.5 MeV. The 5.04 ^{28}Si results and to a lesser extent the 5.04 ^{27}Al results show some discrepancy in the imaginary potential parameters when compared to the parameters found for the rest of the data. It is hoped that these optical model parameters will be useful in analyzing the $(^3\text{He},n)$ data and in Hauser-Feshbach calculations.

Table 3.6

Helion Optical Model Parameters

Nucleus	E	U	r _u	a _u	W	r _w	a _w	σ _r [†]
¹⁹ F	5.0	125	1.07	0.82	11.1	1.8	0.75	577
		*168	1.14	0.77	14.05	1.8	0.66	574
		182	1.07	0.78	13.7	1.8	0.67	560
	6.5	128	1.14	0.75	16.3	1.8	0.76	831
		*144	1.07	0.76	16.1	1.8	0.76	822
		194	1.14	0.69	24.0	1.6	0.77	792
²³ Na	5.0	155	1.14	0.76	10.5	1.84	0.81	456
		*165	1.14	0.70	12.4	1.6	0.99	474
	6.5	125	1.07	0.80	11.97	1.62	0.81	661
		138	1.14	0.45	7.5	1.2	1.64	985
		*166	1.14	0.74	18.5	1.42	0.81	663
²⁷ Al	5.04	118	1.07	0.75	12.6	1.8	0.90	335
		134	1.14	0.39	3.5	1.2	1.84	432
		*171	1.14	0.52	12.2	1.6	1.09	356
	6.5	120	1.07	0.76	7.45	1.94	0.80	579
		157	1.14	0.71	10.9	1.79	0.81	569
		*171	1.07	0.74	10.4	1.81	0.80	566
²⁸ Si	5.04	148	1.07	0.67	1.94	2.49	0.81	261
		*158	1.07	0.58	2.24	1.6	1.68	331
		190	1.14	0.59	1.98	2.53	0.81	279
	6.5	117	1.07	0.77	9.28	1.69	0.81	410
		*152	1.14	0.72	13.12	1.6	0.76	401
		168	1.07	0.73	13.32	1.56	0.81	404

* Indicates parameters used for graphs.

† Reaction cross section.

Figure 3.6 Angular distributions for the elastic scattering of helions from ^{19}F plotted as a ratio of the Rutherford cross-section. The smooth curves are optical model fits to the data generated by the potentials indicated with an asterisk in table 3.6.

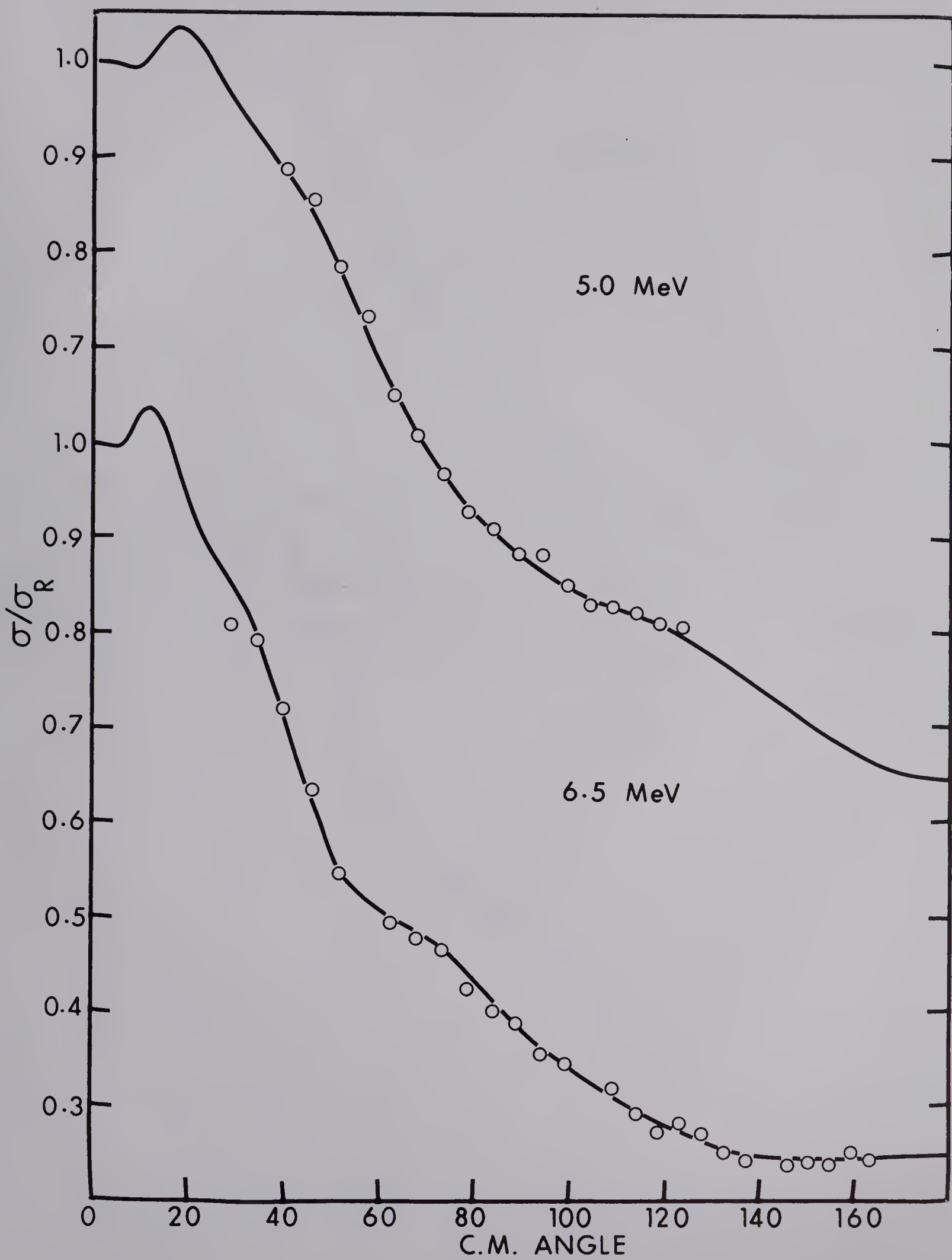


Figure 3.7 Angular distributions for the elastic scattering of helions from ^{23}Na plotted as a ratio of the Rutherford cross-section. The smooth curves are optical model fits to the data generated by the potentials indicated with an asterisk in table 3.6.

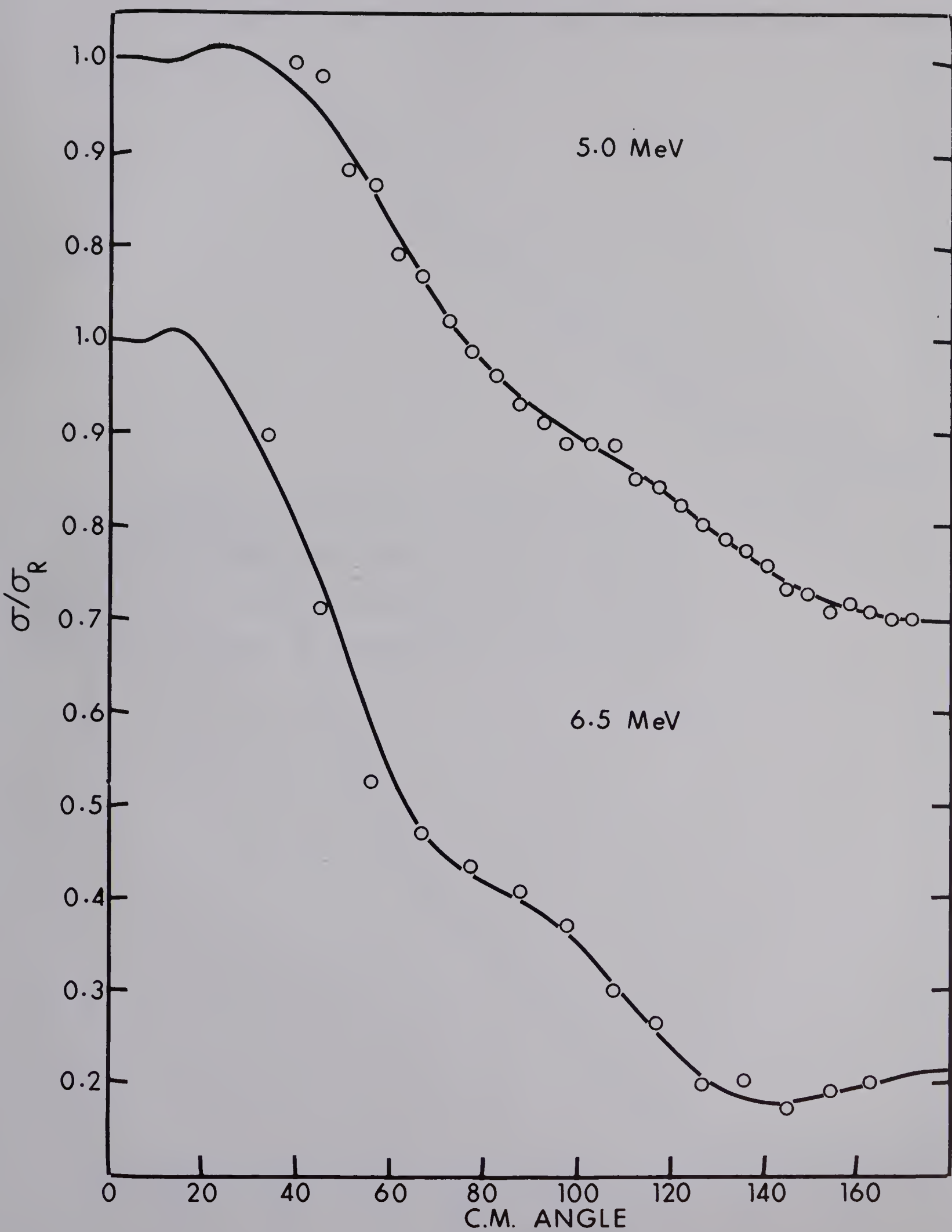


Figure 3.8 Angular distributions for the elastic scattering of helions from ^{27}Al plotted as a ratio of the Rutherford cross-section. The smooth curves are optical model fits to the data generated by the potentials indicated with an asterisk in table 3.6.

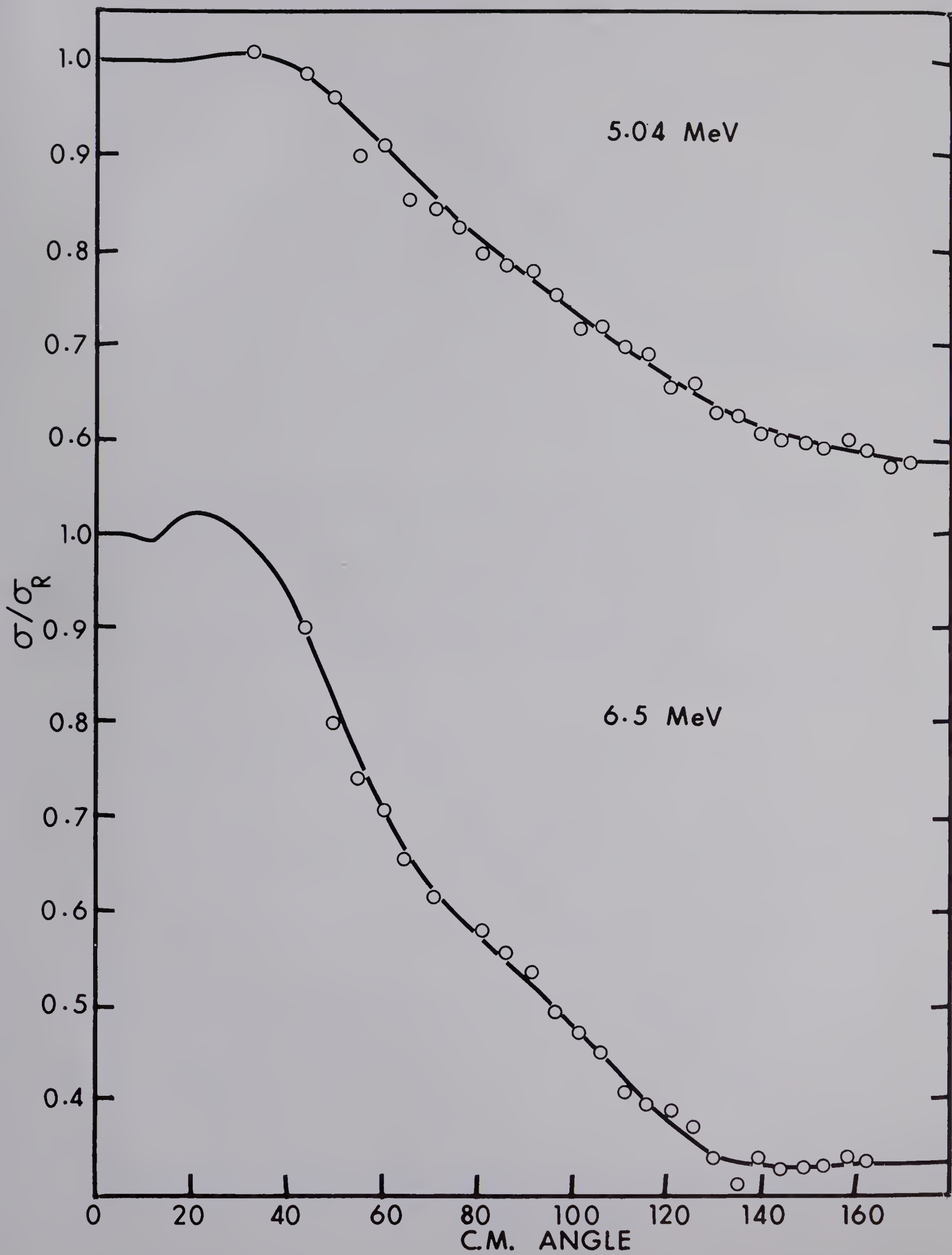
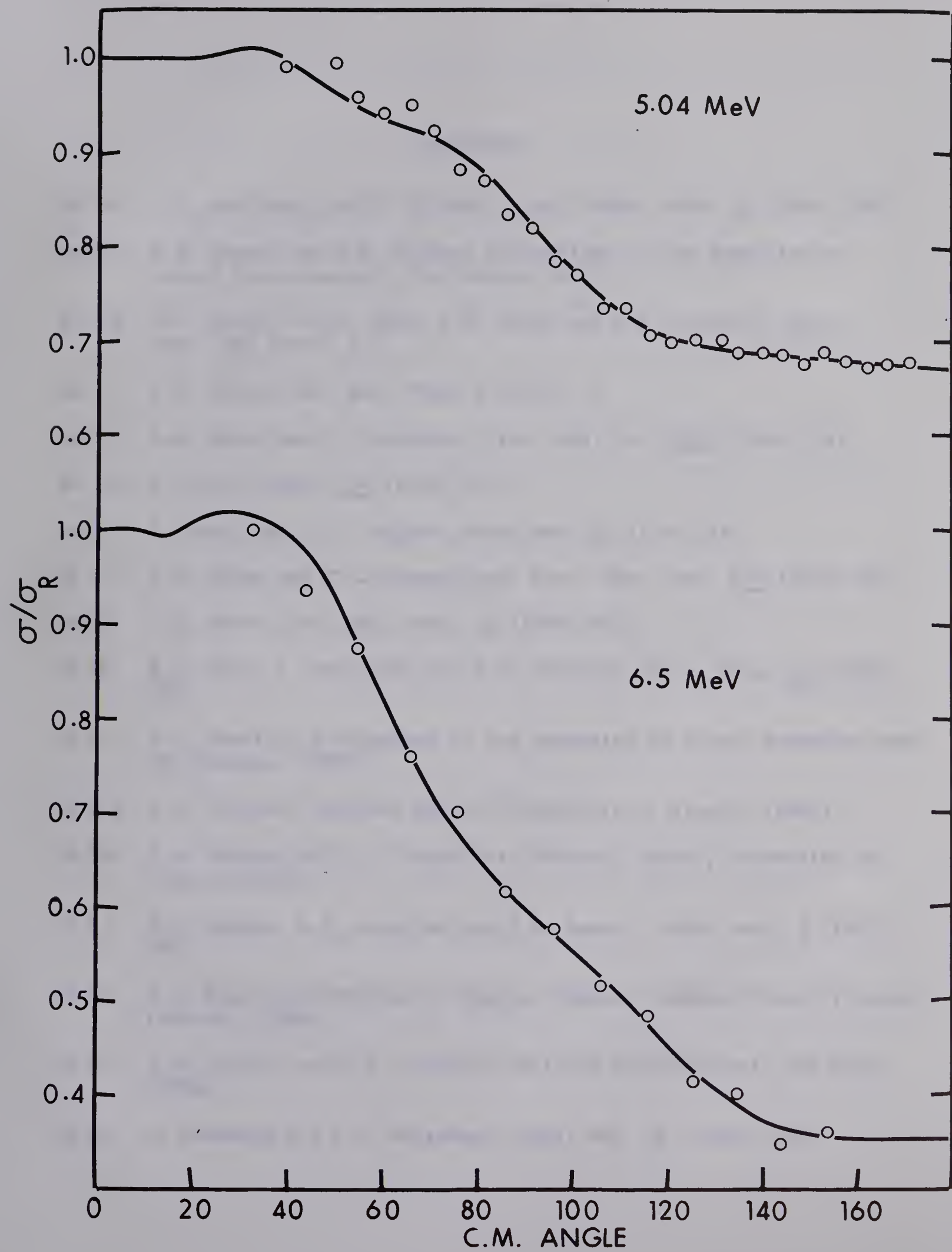


Figure 3.9 Angular distributions for the elastic scattering of helions from ^{28}Si plotted as a ratio of the Rutherford cross-section. The smooth curves are optical model fits to the data generated by the potentials indicated with an asterisk in table 3.6.



REFERENCES

- Ab 66 A.Y. Abul-Magd and M. El-Nadi, Prog. Theor. Phys. 35 (1966) 798
- Ba 67a R.H. Bassel and R.M. Drisko, Proceedings of the Symposium on Direct Reactions with ^3He (Japan), (1967)
- Ba 67b D.J. Baugh, G.J.B. Pyle, P.M. Rolph and S.M. Scarrott, Nucl. Phys. A95 (1967) 115
- Be 37 H.A. Bethe, Rev. Mod. Phys. 9 (1937) 71
- Be 56 H.A. Bethe and J. Goldstone, Proc. Roy. Soc. A238 (1956) 551
- Bo 36 N. Bohr, Nature 344 (1936) 1937
- Br 36 G. Breit and E. P. Wigner, Phys. Rev. 49 (1936) 519
- Br 57 G.E. Brown and C.T. DeDominicus, Proc. Phys. Soc. A70 (1957) 668
- Br 59 G.E. Brown, Rev. Mod. Phys. 31 (1959) 893
- Br 65 K.H. Bray, J. Nurzyński and G.R. Satchler, Nucl. Phys. 67 (1965) 417
- Br 67 D.A. Bromley, Proceedings of the Symposium on Direct Reactions with ^3He (Japan), (1967)
- Da 69a N.E. Davison, Internal Report, University of Alberta (1969)
- Da 69b N.E. Davison and R.G. Humphries, Internal Report, University of Alberta (1969)
- Dr 63 R.M. Drisko, G.R. Satchler and R.H. Bassel, Phys. Lett. 5 (1963) 347
- En 66 H.A. Enge, Introduction to Nuclear Physics, Addison-Wesley (Canada) Limited, (1966)
- Fa 68 A.D. Falkoff and K.E. Iverson, APL/360: User's Manual, IBM Corp. (1968)
- Fe 49 H. Feshbach and V.F. Weisskopf, Phys. Rev. 76 (1949) 1550

- Fe 54 H. Feshbach, C. Porter and V.F. Weisskopf, Phys. Rev. 96 (1954) 448
- Fe 58 H. Feshbach, Ann. Rev. Nucl. Sci. 8 (1958) 49
- Go 64 V.Z. Goldberg, V.P. Rudakov and I.N. Serikov, Congrès International de Physique Nucléaire (Paris) 2 (1964) 908
- Gu 68 D.P. Gurd, Ph.D. Thesis, University of Alberta (1968)
- Ho 56 R. Hofstadter, Rev. Mod. Phys. 28 (1956) 214
- Ho 61a P.E. Hodgson, Proceedings of the Rutherford International Conference (Manchester) (1961) 357
- Ho 61b P.E. Hodgson, Proc. Phys. Soc. 77 (1961) 997
- Ho 63 P.E. Hodgson, The Optical Model of Elastic Scattering, Oxford at the Clarendon Press, (1963)
- Ho 68 P.E. Hodgson, Adv. Phys. 17 (1968) 563
- Ho 69 J.L. Honsaker, to be published
- Hs 68 T.H. Hsu, Ph.D. Thesis, University of Alberta (1968)
- Ma 66 G.M. Matous, G.H. Herling and E.A. Wolicki, Phys. Rev. 152 (1966) 908
- Na 60 M. Namiki, Prog. Theor. Phys. (Japan) 23 (1960) 629
- Pa 68 J.Y. Park, Nucl. Phys. A111 (1968) 433
- Pe 62 F.G.J. Perey and B. Buck, Nucl. Phys. 32 (1962) 353
- Pe 67 F.G. Perey and G.R. Satchler, Nucl. Phys. A97 (1967) 515
- Ro 61 L. Rosenfeld, Nucl. Phys. 26 (1961) 594
- Ro 67 R.R. Roy and B.P. Nigam, Nuclear Physics, John Wiley and Sons, Inc., New York, London and Sydney (1967)
- Ro 69 G. Roy and N. Riebeek, submitted for publication in Nucl. Instr. and Meth.

- Sc 55 L.I. Schiff, Quantum Mechanics, McGraw-Hill Book Company, Inc., New York, Toronto and London (1955)
- Sh 59 H.M. Shey, Phys. Rev. Lett. 2 (1959) 187
- Sh 69 D.M. Sheppard, to be published
- Sm 67 W.R. Smith, private communication
- Su 59 A. Sugie, Prog. Theor. Phys. (Japan) 21 (1959) 681
- Sw 67 L.W. Swenson, R.W. Zurmühle and C.M. Fou, Nucl. Phys. A90 (1967) 232
- Te 66 J.W. Tepel, Nucl. Instr. and Meth. 40 (1966) 100
- Ul 64 I. Úlehla, L. Gomolcák and Z. Pluhar, Optical Model of the Atomic Nucleus, Academic Press, New York and London (1964)
- Vo 62 E. Vogt, Rev. Mod. Phys. 34 (1962) 723
- We 56 V.F. Weisskopf, Physica 22 (1956) 952
- Wi 67 B.H. Wildenthal and P.W.M. Glaudemans, Nucl. Phys. A92 (1967) 353
- Wo 54 R.D. Woods and D.S. Saxon, Phys. Rev. 95 (1954) 577

